

AD A067957

DDC FILE COPY



INSTITUTE
FOR
AEROSPACE STUDIES

UNIVERSITY OF TORONTO

INTERFEROMETRIC TECHNIQUES AND DATA EVALUATION METHODS
FOR THE UTIAS 10 cm x 18 cm HYPERVELOCITY SHOCK TUBE

by

12

G. Ben-Dor and B. T. Whitten

LEVEL

114 110

DDC
APR 27 1979
RESERVED

A

Approved for public release;
distribution unlimited.

March, 1979

UTIAS Technical Note No. 208
CN ISSN 0082-5263

Qualified requestors may obtain additional copies from the Defense Documentation Center, all others should apply to the National Technical Information Service.

Conditions of Reproduction:

Reproduction, translation, publication, use and disposal in whole or in part by or for the United States Government is permitted.

Approved for public release; distribution unlimited.

AIR FORCE OFFICE OF SCIENTIFIC RESEARCH (AFSC)
NOTICE OF TRANSMITTAL TO DDC
This technical report has been reviewed and is
approved for public release IAW AFR 100-12 (7b).
Distribution is unlimited.
A. D. MOSE
Technical Information Officer

INTERFEROMETRIC TECHNIQUES AND DATA EVALUATION METHODS
FOR THE UTIAS 10 cm x 18 cm HYPERVELOCITY SHOCK TUBE

by

G. Ben-Dor and B.T. Whitten

REVISION BY	
RTM	WHM/WHM
DDG	DDG/WHM
UNANNOUNCED	
JUSTIFICATION	
BY	
DISTRIBUTION/AVAILABILITY CODE	
Dist.	AVAIL. DIST. SPECIAL
A	

March, 1979

UTIAS Technical Note No. 208

Acknowledgement

We wish to thank Professor I.I. Glass for the opportunity to work with him and learn from him.

Sincere thanks are offered to Mr. W.L. Buchanan for proofreading this report.

The assistance received from Mrs. L. Quintero in drawing the figures and Ms. B. Waddell in typing this report is very much appreciated.

This work was supported by the U.S. Airforce under Grant AFOSR-77-3303 and the National Research Council of Canada.

Abstract

The UTIAS 10 cm x 18 cm Hypervelocity Shock Tube has been used in recent years to study ionizing shock structures, flat-plate and side-wall boundary layers and nonstationary oblique shock-wave diffractions over compression corners. These phenomena were recorded using a 23-cm dia field of view Mach-Zehnder interferometer equipped with a giant-pulse dual-frequency ruby laser.

In order to extract the maximum amount of data in these complex flows a digital evaluation method was employed. For this technique a new approach to the theory of interference was developed. In this approach the spatial coordinates (x,y) of the various lines of interference (fringes) on the interferograms are put into digital form, thereby making a computer analysis possible.

The experimental technique and instrumentation associated with the various measurements involved in research using the UTIAS 10 cm x 18 cm Hypervelocity Shock Tube are described. Finally, the maximum possible absolute and relative errors associated with these measurements are calculated for four different gases (argon, krypton, oxygen and nitrogen) which are usually used as test gases.

Table of Contents

	<u>Page</u>
Abstract	iii
Notation	v
1. INTRODUCTION	1
2. UTIAS 10 cm x 18 cm Hypervelocity Shock Tube	1
2.1 Shock Tube Driver	1
2.2 Basic Instrumentation	6
2.3 Accuracy of Measurements	10
2.4 Mach-Zehnder Interferometer	13
3. PRINCIPLES OF TWO-WAVELENGTH INTERFEROMETRY	20
3.1 Absolute Errors	24
4. SPATIAL ANALYSIS OF INTERFEROGRAMS	27
5. CONCLUSIONS	39
REFERENCES	40
TABLES	
FIGURES	

Notation

a	entrance position to test section
a	speed of sound
Ar	argon atom
Ar ⁺	argon ion
b	exit position from test section
c ₀	speed of light in vacuum
d	unsupported diameter of the diaphragm = 18.1 cm
e	electron charge
E(ϕ)	absolute error in measuring quantity ϕ
H	the height difference of the oil in the manometer
g	standard acceleration of gravity (= 980.665 cm/sec ²)
h	residual thickness of the diaphragm after scribing (Eq. 1.2)
k	arbitrary constant
K	constant (Eq. 1.2)
K _j	Gladstone-Dale constant of species j
Kr	krypton
l	geometrical length travelled by light section
L	geometrical distance across test section
m _j	mass of species j
M	continuous fringe number
M'	integer fringe number
M _s	incident shock-wave Mach number
n	index of refraction
n	constant (Eq. 1.2)
n _j	number density of species j
N	continuous variable

Notation - continued

N'	integer variable
N_2	nitrogen molecule
O_2	oxygen molecule
P	pressure
P_{burst}	bursting pressure of the diaphragm
P_1	initial pressure ahead of the diaphragm
P_4	P_{burst}
R	gas constant
S	fringe shift
S	distance between two shock detectors
t	time
t	total diaphragm thickness (Eq. 1.2)
T	temperature in $^{\circ}K$
T_0	initial temperature
T_L	laboratory temperature
V_s	velocity of incident shock wave
x	spatial coordinate
X	collision partner
y	spatial coordinate
z	spatial coordinate
α	degree of dissociation
β	induced electric dipole polarizability of the gas
γ	specific heats ratio $= (C_p/C_v)$
δ	first variation of an integral
$\Delta\phi$	change in property ϕ
ϵ	angle of rotation of second beam splitter in interferometer

Notation - continued

θ_w	wedge angle
λ	light source wavelength
λ_o	light source wavelength in vacuum
ρ	density
ρ_{oil}	density of the oil in the manometer
τ	optical path length
τ^*	optical path length inside the test section
ω	light source frequency
ω_p	plasma frequency
χ	degree of ionization

Subscripts

a	atom
e	electron
E	ionization equilibrium conditions
i	ion
m	molecule
p	test section arm of the interferometer
q	compensation chamber arm of the interferometer
r	reference point
o	"no-flow" conditions

1. INTRODUCTION

The UTIAS 10 cm x 18 cm Hypervelocity Shock Tube was built in 1965 and reported in detail (design, instrumentation and performance) by Boyer (Ref. 1) upon completion of the construction and calibration. In addition Bristow (Ref. 2) reported on further modifications and improvements.

Since then, further modifications and changes were made by various researchers who have used the facility for investigating dissociating and ionizing gases and various shock-wave phenomena.

Since the original design was in British units, which were replaced recently by the metric system, and since the various modifications are described in various UTIAS publications, it was felt necessary to combine them all together in an updated document that will describe the present status of the shock-tube as well as its maintenance and operation procedures.

The investigated phenomena are usually recorded using a 23 cm dia field of view Mach-Zehnder interferometer equipped with a dual-frequency giant-pulse laser. Consequently, the basics of two-wavelength interferometry are reviewed, and a new and very accurate interferometric data-evaluation method is presented.

2. UTIAS 10 cm x 18 cm HYPERVELOCITY SHOCK TUBE

The UTIAS combustion driven hypersonic shock tube is a large, well-constructed facility, approximately 15 meters in length, designed to simulate high enthalpy, real gas flows typical of hypersonic flight. The combustion driver is capable of generating shock speeds in excess of 7 kilometers per second. A detailed account of the component design and construction features has been given by Boyer (Ref. 1), while improvements and modifications to the system have since been reported by Bristow (Ref. 2).

A schematic overview of the shock tube facility in its present form is shown in Figure 1. In describing the major components and operation, an attempt is made, where possible, to convert the dimensions of feet and inches from the original design to more conventional metric units.

2.1 Shock Tube Driver

The chrome-molybdenum steel cylindrical driver has an internal diameter of 15.24 cm (6") with a wall thickness of 10.16 cm (4"), and can withstand pressures up to 11,000 psi with a safety factor of 6. A driver length of 1.422 m (56") was considered adequate and economical for the experiments, although other lengths are available. Driver pressures up to about 1000 psi are usually acquired directly from gas bottles while higher pressures are obtained by the combustion of a stoichiometric mixture of hydrogen and oxygen, diluted with helium. The optimum mixture used for smooth combustion and relatively fast rise time was determined by Bristow (Ref. 2), which consisted of 7.5% oxygen, 20% hydrogen (includes 5% used as a partial diluent) and 72.5% helium by pressure. As indicated by Benoit (Ref. 3), the pressure should increase by a factor of about 8 upon combustion, although experiments have shown this factor to be around 6.7. Consequently, a conservative estimate of 6.1 was used, giving an insurance factor of 10% when determining the correct mixture pressure for a particular diaphragm

bursting pressure.

The combustion is achieved by heating a long, 0.38 mm (0.015") diameter tungsten wire, suspended over the length of the driver along the centre-line. To obtain the necessary wire temperature, a 4.5 μ f capacitor, maintained at 13.4 Kv, is discharged through a triggered gas-type spark gap and the wire to ground. Poor ignition is minimized by adequately insulating the high voltage connection through the driver wall with a continuous 4 mm thick, teflon sheath, and ensuring a bright yellow glow of the wire under atmospheric testing.

To obtain excellent repeatability and control of the combustion pressure, the driver is evacuated to approximately 1 torr prior to each experiment, using a Cenco, Hyvac 14, mechanical vacuum pump. The correct amount of oxygen for the final mixture is then admitted and critically monitored to ± 0.1 psi using a Heise, H17507C, dial pressure gauge. Helium is then added to reach 46% of the mixture pressure, hydrogen to reach 66%, and finally helium again to complete the mixture. By using this sequence and admitting all gases through a mixing tube with small orifices every 15 cm along the complete length of the driver, excellent combustion performance is ensured.

Diaphragms

The diaphragm clamp between the driver and driven sections is designed for diaphragm discs, 35.4 cm in diameter (13.875"), and leaves an unsupported diameter of 18.1 cm (7.125"). O-rings seal against the supported annulus of the diaphragm on each side. Two types of diaphragm can be used. For non-combustion driver pressures less than 1000 psi ($M_0 < 10$) mylar discs are cut from sheets ranging in thickness from 0.001" to 0.050". For the unsupported diameter of 18.1 cm, mylar was found experimentally to have a bursting pressure, varying linearly with thickness, as

$$P_{\text{burst}} = 7300t \pm 8\% \text{ psi} \quad (1.1)$$

where t = mylar thickness in inches. Consequently, desired bursting pressures can be achieved merely by combining discs of various thickness. It should be noted that the mylar diaphragms burst without shattering, leaving the tube free from debris. The longer formation distance caused by a slower opening is not a problem in this long facility.

The stronger shock waves are generated using annealed, stainless steel, type 304 (SS 304) diaphragms with a 2-B finish to provide adequate vacuum sealing. These diaphragms are machine-scribed in the form of a 90° cross on the driven side to enable petaling rather than shattering when burst by the combustion pressure. General thicknesses in the range 0.062" to 0.182" are sufficient to cover the range of necessary bursting pressures for $10 \leq M_0 \leq 18$ by machining the scribe depth appropriately. For each diaphragm, the bursting pressure can be predicted from the calibrations of Bristow (Ref. 2) as:

$$P_{\text{burst}} = K \left(\frac{4\sigma t}{d} \right) \left(\frac{h}{t} \right)^n \text{ psi} \quad (1.2)$$

where

t - total diaphragm thickness

h - residual thickness of the diaphragm after scribing,

d - unsupported diameter of the diaphragm = 18.1 cm,

σ - ultimate tensile strength of the annealed material,
which for SS 304 is 85,000 psi.

The remaining parameters were found experimentally from the calibration as:

$$n = 2.2 \pm 0.1$$

$$K = 1.01 \text{ for } t = 0.172" \text{ and } d = 18.1 \text{ cm}$$

$$K = 1.10 \text{ for } t = 0.109" \text{ and } d = 18.1 \text{ cm}$$

$$= 1.06 \text{ for } t = 0.062" \text{ and } d = 18.1 \text{ cm}$$

To ensure proper petaling, the ratio of residual thickness to total thickness is kept between $0.55 \leq h/t \leq 0.75$. The variation in total thickness over each diaphragm is kept below 0.004" while the residual thickness is machined to an accuracy of ± 0.0005 " using a vacuum chuck. These rigid tolerances are maintained both for safety and for repeatability of experiments. Machining details have been outlined by Boyer (Ref. 1).

For optimum performance, the diaphragm is chosen to have a bursting pressure equal to the driver pressure p_h required to drive a shock wave at specified Mach number M_s into the test gas at specified initial pressure p_1 . Hydrogen, helium and carbon dioxide are usually used as the driver gases for obtaining shock waves in the range $2 \leq M_s \leq 10$ with mylar diaphragms.

In this case, the bursting pressure is determined from standard curves relating the required pressure ratio p_h/p_1 , to the desired Mach number M_s (Ref. 4) with a correction factor of about 2 used to account for non-ideal effects. A recommendation of driver/driven gas combinations and the required pressure ratio p_{h1} for incident shock waves in the range $2 \leq M_s \leq 8$ for oxygen, nitrogen and argon as test gases is given in Table 1. For combustion driver experiments into argon Bristow (Ref. 2) developed the following empirical expression

$$\ln \left(\frac{p_h}{p_1} \right) = 0.422 M_s + 4.02 \quad 10 \leq M_s \leq 24$$

A different expression was claimed by Whitten:

$$\frac{p_4}{p_1} = 1350 (M_s - 10)^2, \text{ for } 12 \leq M_s \leq 18$$

Unfortunately, a similar expression for krypton was not developed, due to the lack of sufficient number of experiments. However, Tang (Ref. 5) established an empirical relation for $M_s \approx 15$

$$\ln \left(\frac{p_4}{p_1} \right) = (0.422 M_s + 2.92)$$

Note that p_4 in the above mentioned expression is P_{burst} as calculated from Eq.(1.2).

Shock-Tube Driven Section

As shown in Figure 1 the driven section, made from SPS-245 tool steel, has a total length of 15.24 m (50'), including a 0.457 m (1.5') transition section from circular to rectangular cross-section, and a specially designed 1.2192 m (4') test section located 13.56 m (44.5') from the diaphragm station. It is terminated by a large dump tank in the form of a vertical cylinder with hemispherical caps whose internal diameter is 0.9144 m (3'), overall height is 1.93 m (6.5') and whose volume is 1 m³ (35.4 ft³). The rectangular channel cross-section, as indicated, has a horizontal width of 10.16 cm (4") and a vertical height of 17.78 cm (7"). The internal surfaces were originally ground to a 0.8 micron (32 microinch) finish and plated with a 51 micron (.002") layer of chromium. Instrumentation ports, lettered A, B, C, ... (Figure 1) are located at 1.2192 meter (4') intervals along the driven section allowing for installation of necessary gauges.

The test section contains 6 instrumentation ports, and incorporates two interferometric quality circular windows, basically 20.32 cm (8") in diameter and 9.53 cm (3.75") thick. These windows were made from borosilicate crown (BK-7) optical quality glass, with surfaces ground and polished flat to within a wedge angle less than 2 seconds of arc, and specified to have a maximum peak to peak variation in transmitted wavefront over the entire diameter of less than one-quarter of a wavelength at 6328 Å. These rather large windows were very carefully mounted in frames, with flat neoprene rubber vacuum gaskets and 25 micron removable shims used to prevent any metal to glass contact. The sensitive mounting is important with this size of window in preventing any undue stress concentration and cracking from either the shock loading or the initial mounting itself, and essential from the standpoint of safety, economics and interferometric quality.

Surface burns and deposits that might develop on the windows, particularly near any perpendicular metal surfaces (test models) are often removed using a dilute solution of hydrochloric acid, and were, if necessary, moved from a particular region of interest by a 180° rotation of the rectangular window frames.

The entire driven section and dump tank, comprising a volume of 1.28 m^3 (45.13 ft^3), are evacuated prior to each experiment to maintain the highest possible purity of the test gas under consideration. The pumping system includes, in series, a Kinney type KS-47 mechanical pump, a Heraeus Roots, type RG-350, blower (forepump) and a CVC, type PMCS-6B, six-inch diameter diffusion pump. The ultimate vacuum after a pumpdown period of about three days was 3×10^{-5} torr, with a leak-outgassing rate of 2×10^{-5} torr per minute. The slightly longer pumping time than that reported by Bristow (Ref. 2) can be attributed to a modification of the coupling between the vacuum pump system and the shock tube. Previously, the vacuum manifold had been connected to the tube by three pipes, 5.08 cm (2") in diameter, to ports situated between 1.5 m and 2.7 m from the diaphragm station. A high pressure and vacuum service ball valve was located on each pipe, approximately 21.3 cm from the interior wall of the shock tube, allowing a total cavity volume of 1240 cm^3 to the tube at all times. In view of the instabilities observed by several experimenters in this facility for strong ionizing shock waves in argon, it was useful to eliminate any possible contributing factors, no matter how remote. Consequently, only one port was retained, with the ball valve modified to lie about 5 cm from the interior wall. The remaining ports were blanked off leaving an exposed cavity volume of 103 cm^3 , or one-tenth of the original cavity. Although no noticeable differences were observed with the shock stability problem, the single connection was retained as the more appropriate system, particularly since the conductance loss did not seriously affect the pumpdown time.

Test Gas Conditions

To ensure a reasonable degree of cleanliness before each experiment, a general procedure is followed in which the driven section is purged with high pressure air, the test section windows (in their frames) are removed and cleaned with optical solution, and the test section walls are scrubbed in succession with trichloroethylene, acetone and finally methyl alcohol. (On occasion, the entire driven section is cleaned in this manner). As mentioned, the driven section is then evacuated over a period of usually three days. Before the introduction of the test gas, the pressure is monitored by an ionization gauge (Associated Electrical Industries, Model VC-10) located at an instrumentation port, 2.4 m from the diaphragm station. The pressure in the vacuum manifold can also be checked with a CVC type GPH-100A discharge gauge. A pressure of less than 5×10^{-5} torr is generally required before proceeding with an experiment. A mass spectrometric investigation of the driven section under these conditions indicated the pressure to be made up mainly of water vapour (70%), nitrogen (20%) and oxygen (5%). In addition, the leak rate after isolation of the vacuum pumps was found to be approximately 2×10^{-5} torr/minute, with the increase in pressure due almost entirely to air (N_2 and O_2).

In the experimental procedure, the test gas is admitted immediately after isolation of the vacuum pumps to minimize effects of outgassing, and the shock tube is "fired" approximately 2 to 5 minutes following this. Hence, a maximum impurity partial pressure of about 2×10^{-4} torr is ensured, which, for a relatively low initial pressure of 5 torr, amounts to an impurity level of 40 ppm. As the test gas is admitted to the driven section, the pressure is monitored at the vacuum manifold with a Wallace and Tiernan, type FA 160 (0-50 torr) dial gauge. A more accurate measurement of the initial pre-shock pressure is then made using an oil manometer (0.2-40 torr),

described by Bristow (Ref. 2). This device consists of a 50 cm long, 1 cm inside-diameter, glass U-tube with, at one end, a bulb reservoir containing Dow Corning, DC 704 diffusion pump oil, and at the other, a flexible connection to the system. The manometer is vacuum pumped before use, keeping the oil in the reservoir by a 120° rotation of the tube. In the upright position, pressure can then be determined simply by a sensitive measurement of the height difference H, between oil levels in each arm, i.e., $p = \rho_{oil} gH$ dynes/cm², where $g = 980.655$ cm/sec² (standard acceleration of gravity)

$\rho_{oil} = 1.069 + 9.5 \times 10^{-4} (25^\circ\text{C} - T) \text{g/cm}^3$, is the density of DC 704 oil, adjusted about 25°C for thermal expansion.

T is the oil temperature in the manometer.

In units of torr, $p = \rho_{oil} H / 13.5951$ where H is measured in mm.

The temperature of the driven section is measured to an accuracy of $\pm 0.1^\circ\text{C}$ prior to each experiment using a standard mercury bulb thermometer, inserted in a 5 cm deep, 6 mm diameter oil-filled port in the upper wall of the shock tube walls, this measurement is taken as the initial pre-shock temperature of the test gas.

2.2 Basic Instrumentation

Fast-response electronic equipment is used to monitor the shock-tube performance in each experiment. This includes a shock detection system for both accurate measurement of shock velocity and microsecond control of the diagnostic equipment, and the recording of pressure history in both the driver and driven sections.

Shock Detection

In each experiment, the arrival of the shock front at several locations along the driven section is detected using Atlantic Research, type LD-25, piezoelectric pressure transducers, flush mounted in selected instrumentation ports. These gauges have a sensitivity of approximately 0.15 V/psi, a rise time less than 1 microsecond, and, as shock detectors, require a minimum amount of associated electronic equipment. The 6 mm diameter surface of each gauge is given additional protection with a thin coating of silicone rubber (GE RTV).

The transducer output is connected directly to a power preamplifier*, situated immediately adjacent to the gauge, which consists simply of a field-effect transistor for high-impedance input as a source follower, and a one-stage emitter-follower. Although the voltage gain is less than unity, the power gain and low impedance output enables the subsequent transmission through long lengths of cable with no appreciable signal loss. If necessary, the signal is increased in voltage at the main electronics console by a small, two-stage, resistance-coupled amplifier* which uses a "diode-catching" technique to give a 20-volt output for all amplified signals greater than a pre-set level, and 0 volts for any lower signals. Correct

* Courtesy of Mr. A. Perrin, UTIAS

3

selection of this level before each experiment effectively discriminates against anticipated input noise, and the 20-volt output signal is suitable, for example, in triggering conventional electronic counters. The overall response time of the system is less than 1 microsecond. The transducer, along with relatively minor electronic equipment, provides an economical, reliable and accurate method of shock detection with proven durability. The system schematic is included for general information in Figure 2.

The detectors were used both in the measurement of shock velocity and in the accurate timing of the laser light source for interferogram exposure discussed in Section 2.4.

Shock Velocity Measurements

The incident shock velocity is monitored using an x-t arrangement (a typical arrangement is shown in Fig. 3). Three Hewlett-Packard (Type 3734A) and two Racal (Type SA.45) digital counters are connected to a common, external, one megacycle oscillator giving all counters a uniform time base with a one microsecond resolution. When the shock wave arrives at station D, (8.5 m downstream of the diaphragm and 5.7 m upstream of the test section) time counters 1,2,3,4 and 5 are triggered simultaneously. These five counters are then stopped in succession as the shock-wave passes subsequent detectors at stations F,G,H,I and J. An additional Hewlett-Packard (Type 5325 A) counter (No.7, Fig.3) is used between stations I and J to indicate the time taken for the shock-wave to travel past the test section and the test model. Since the shock-wave velocity changes somewhat due to diffraction over test models (Refs. 6 and 7), the measurement of counter No.7 is used only as a monitor of the shock location.

The control of the laser light source operation is also included in Fig. 3. The laser-flashlamp capacitor bank is usually triggered by the shock arrival at station F, suitably delayed in a Tetronix type 555 oscilloscope to get 900 microseconds of energy-pumping-time by the time the Pockels-cell shutter opens. The Pockels cell Q-switch is always triggered from station I, delayed correctly in a pulser delay unit to take the interferogram at a desired time (or location of the shock wave wrt station I).

To monitor the actual flashlamp pumping time in each experiment, synchronization pulses from both the flashlamp capacitor bank and the Pockels-cell pulser unit are used to start and stop, respectively, a UTIAS microsecond counter (Fig. 3, Counter No.6).

As an additional check on shock-tube performance in each experiment, a Kistler type 601-B, piezoelectric pressure transducer is used to monitor the pressure variation with time behind the incident shock wave. The transducer output is taken directly to a charge amplifier (Kistler, Model 504) with a final signal displacement on the designated oscilloscope (Fig. 3).

With the above configuration, an x-t plot for a typical experiment is shown in Fig. 4, with the (0,0) reference taken as station D.

The shock velocity along the driven section is determined in two ways. The average velocity between stations is immediately obtained by finding the slope of straight line segments joining successive points (i.e., a simple division of the distance between stations by the difference in

the recorded shock arrival times at respective locations). The error in this measurement depends on the maximum spatial uncertainty of ± 6 mm arising from the finite size of the shock detectors, and the ± 1 μ sec uncertainty in time recording. For the closest inter-station distance of 0.61 m, and a time measurement of 110 μ sec for a typical shock speed of 5500 m/sec, the error in measured average shock velocity would be, at most, 2% (see subsequent discussion in Section 2.3).

A smooth curve is also fitted to the set of (x,t) points by a method of least-squares using Chebychev polynomials. The best fit of lowest order satisfying the uncertainties in each point is determined numerically, and the result, in most cases, is a parabolic or second order fit. The instantaneous shock-wave velocity could then be evaluated from the derivative at anytime or position. Unfortunately, the differentiation of such a fit always involves a loss of accuracy which is somewhat difficult to quantify, particularly with only five data points involved. However, with the smooth fit satisfying the uncertainties in all points, it is felt that this method is slightly better than the calculation of average velocities, with the accuracy estimated to be under 1% within the bounds of the data.

Past examination of the instantaneous and average velocities along the driven section indicated that the shock speed was decreasing or attenuating as expected. For example, over the length of 5.49 m (between stations D and I), the maximum observed change in wave speed was found to be 5% (often, it is much less). In other words, the maximum attenuation is less than 1% per meter, and just above the uncertainties in the velocity measurements themselves. As a result, for each experiment, the shock velocity used in ensuing calculations is taken as the mean value of the instantaneous velocity determined at station I immediately ahead of the test section, and the average velocity between stations H and I. The uncertainty in shock Mach number from this calculation should be less than 1%.

Pressure Measurements

As an additional check on the shock tube performance in each experiment, two Kistler type 601-B, piezoelectric pressure transducers (acceleration-compensated) are used to monitor the pressure variation with time in the driver and driven sections respectively. The transducer output in each case is taken directly to a charge amplifier (Kistler, Model 504) with the final signal displayed on a designated oscilloscope as shown in Fig. 3.

The combustion driver pressure transducer is mounted on the closed end of the driver section and given a 2 mm thick surface coating of silicone rubber (G.E. RTV) for additional protection from the higher sustained combustion temperatures. A typical combustion trace is shown in Fig. 5a in which the sweep is triggered as the capacitive discharge began through the tungsten ignition wire. The first portion of the trace remains level at the pre-combustion mixture pressure (423 psi in this case) where the original base-line position before introduction of driver gas has been indicated. (The measurement of mixture pressure is only possible by using the long time constant setting of the charge amplifier and can be maintained for only a period of perhaps 3 minutes). In this experiment, a time of about 4 milliseconds elapsed before the wire was sufficiently hot to initiate combustion. The small perturbation of the signal at the beginning of the pressure trace is believed to be noise as a result of the electrical discharge through the

wire and not a real pressure pulse, particularly since several perturbations of this kind were observed whenever the wire was found to have broken during combustion.

The pressure is then seen to rise smoothly until the arrival of the nonstationary rarefaction wave indicating the breakage of the diaphragm. In this experiment, the diaphragm was scribed to burst at a pressure of 2452 psi, while the combustion pressure at the closed end appeared to reach about 2500 psi, possibly indicating a slight "over-driving" of 2%. This is probably a result of the 10% safety factor used to ensure diaphragm burst as discussed previously, and appears inconsequential to the desired results. The combustion pressure measurements are used to ensure that correct driver performance is obtained in each experiment, and results substantiated that by following the careful driving techniques outlined in Section 2.1, excellent control and repeatability could be obtained.

The driven section pressure transducer is flush-mounted in the selected instrumentation port (Station M in Fig. 3). Because of the extremely rapid pressure change across the shock front, a significant amount of noise is superimposed on the output signal by the oscillation or "ringing" of the transducer diaphragm whose resonant frequency appeared to be around 150 Kc, consequently, the noise is reduced by passing the amplified signal through a 100 Kc filter, although this limits the rise-time to about 10 microseconds and hence excludes measurements near the shock front itself.

Figure 5b shows the pressure trace obtained for a shock wave travelling at Mach number of 15 into an initial argon pressure of about 6 torr. The small oscillations on the trace are the filtered result of the aforementioned "ringing" and are more intense for stronger shock waves as expected. Using the velocity measurements to determine shock Mach number at station M, the frozen (immediately behind the shock front) and equilibrium pressures predicted from the Hugoniot shock jump conditions are indicated. It is seen that the pressure soon after the initial rise is predicted well by the equilibrium shock jump conditions.

The initial frozen pressure is not measured accurately in comparison, because of the finite rise-time of 10 μ sec. However, the fact that a relaxation time does exist in which the pressure changes from a frozen to an equilibrium value is seen by a change in the slope of the initial pressure rise. In Fig. 5b a small "kink" is visible as the pressure appears to rise over a time of approximately 10 μ sec. Accurate interferometric measurements made simultaneously showed the actual relaxation time to be only 5 μ sec for this experiment ($M_s = 15$) which is less than the rise-time of the system and hence cannot be resolved.

The pressure is seen to remain essentially constant. A decrease in pressure would be an indication of the arrival of the contact surface, or the reflected rarefaction wave from the driver.

The accuracy of the driven pressure measurements, allowing for gauge calibration factor, charge leakage and ringing is estimated to be around 10%. The traces in each experiment are used principally to verify the shock jump conditions calculated from the measured shock Mach number, indicate the available test time (and possibly the relaxation time), and generally ensure that conditions through the shock wave are as expected.

2.3 Accuracy in Measurements

In general, measurements are divided to direct and indirect. The temperature, for example, is measured with a standard mercury bulb thermometer and hence it is being measured directly, while the shock-wave velocity is obtained through time and distance measurements, and therefore an indirect measurement method is applied.

While indirect measurements the errors arise: strictly from the resolution of the measuring device, and hence, are very easy to estimate (usually given), the approximation of the error involved in an indirect measurement is more complicated. In the following the absolute errors involved in measuring the incident shock-wave Mach number M_s and the initial pressure P_0 , are evaluated. Note that these errors are the maximum possible errors, and hence in general the actual errors are much less.

Incident Shock-Wave Mach Number M_s

The incident shock-wave Mach number is defined as

$$M_s = \frac{V_s}{a} \quad (2.1)$$

where V_s is the shock-wave velocity and a is the speed of sound ahead of it. Thus, the accuracy in calculating M_s depends on the accuracy of measuring V_s and a . However, V_s and a cannot be measured directly, they are obtained from

$$V_s = \frac{s}{t} \quad (2.2)$$

$$a = \sqrt{\gamma RT} \quad (2.3)$$

where s is the distance between two shock detectors, t is the measured time in which the shock wave travels the distance s , and T is the temperature of the quiescent gas ahead of the shock wave.

The uncertainty associated with the direct measuring of s , t and T are:

$$dT = \pm 0.1^\circ \text{ K}$$

$$dt = \pm 1 \times 10^{-6} \text{ sec.}$$

$$dS = \pm d/2 = \pm 0.3 \text{ cm}$$

where d is the diameter of the shock detectors.

Consequently, the absolute errors associated with these measurements are:

$$E(T) = 0.2^{\circ}K$$

$$E(t) = 2 \times 10^{-6} \text{ sec}$$

$$E(s) = 0.6 \text{ cm}$$

where $E(\phi)$ indicates the absolute error associated with measurement " ϕ ".

Using the elementary error approximations, one obtains from Eqs. 2.1 to 2.3.

$$E(M_s) = \frac{1}{a} E(V_s) + \frac{V_s}{a^2} E(a) \quad (2.4)$$

$$E(V_s) = \frac{1}{t} E(s) + \frac{s}{t^2} E(t) \quad (2.5)$$

$$\frac{E(a)}{a} = \frac{1}{2T} E(T) \quad (2.6)$$

Inserting Eqs. 2.5 and 2.6 into Eq. 2.4 yields

$$\frac{E(M_s)}{M_s} = \frac{E(s)}{s} + \frac{E(t)}{t} + \frac{1}{2} \frac{E(T)}{T} \quad (2.7)$$

Equation 2.7 can be rewritten in a slightly different form

$$\frac{E(M_s)}{M_s} = \frac{E(s)}{s} + M_s \frac{s}{s^2} E(t) + \frac{1}{2} \frac{E(T)}{T} \quad (2.8)$$

Typical values of T and a are

$$T = 300K$$

$$a = 321 \text{ m/sec for argon}$$

$$a = 223 \text{ m/sec for krypton}$$

$$a = 328 \text{ m/sec for oxygen}$$

$$a = 351 \text{ m/sec for nitrogen}$$

Taking the shortest s for which the shock tube velocity is measured, to get the largest possible error, and inserting the appropriate values into Eq. 2.8 result in:

$$\frac{E(M_s)}{M_s} = (1.05 M_s + 10.18) \times 10^{-3} \quad \text{for argon}$$

$$\frac{E(M_s)}{M_s} = (0.73 M_s + 10.18) \times 10^{-3} \quad \text{for krypton}$$

$$\frac{E(M_s)}{M_s} = (1.08 M_s + 10.18) \times 10^{-3} \quad \text{for oxygen}$$

$$\frac{E(M_s)}{M_s} = (1.15 M_s + 10.18) \times 10^{-3} \quad \text{for nitrogen}$$

Note that the relative error $E(M_s)/M_s$ increases as M_s increases.

Initial Pressure P_o

Initial pressures in the range $0.2 \leq P \leq 40$ tor. are measured by an oil manometer. The pressure P_o is obtained from the relation

$$P_o = \frac{\rho_{oil} \times H(\text{mm})}{13.5951} \quad (2.9)$$

where H is the oil-height difference measured in the manometer ρ_{oil} is the density of the oil and it is given by:

$$\rho_{oil} = 1.0690 + 9.5 \times 10^{-4} (25-T) \quad (2.10)$$

T is the oil temperature in centigrad. The oil temperature is not measured directly, however, it is assumed that it is equal to the room temperature near it, ($T = T_L$).

Using the elementary error approximation, Eqs. 2.9 and 2.10 can be rewritten as

$$E(P_o) = \frac{1}{13.5951} \left\{ H(\text{mm}) E(\rho_{oil}) + \rho_{oil} E[H(\text{mm})] \right\} \quad (2.11)$$

$$E(\rho_{oil}) = 9.5 \times 10^{-4} E(T_L) \quad (2.12)$$

Inserting Eq. 2.12 into Eq. 2.11 results in:

$$E(P_o) = \frac{1}{13.5951} \left\{ 9.5 \times 10^{-4} H(\text{mm}) E(T_L) + \rho_{oil} E[H(\text{mm})] \right\} \quad (2.13)$$

Substituting the following values,

$$E(T_L) = 0.2^\circ K$$

$$\rho_{oil} = 1.069 \text{ g/cm}^3$$

$$E(H) = 1 \text{ mm}$$

Into Eq. 2.13 results in:

$$E(P_o) = 1.398 \times 10^{-5} H(\text{mm}) + 7.863 \times 10^{-2} \quad (2.14)$$

The range of pressures under consideration ($0.2 \leq P_o \leq 40$ torr) corresponds approximately to $2 \leq H \leq 500$ mm, thus the maximum errors associated with initial pressures of 0.2 and 40 torr are 0.079 torr and 0.086 torr, respectively. For a laboratory temperature of 25°C Eqs. 2.9 and 2.10 can be used to reduce Eq. 2.14 to:

$$E(P_o) = 1.778 \times 10^{-4} P_o + 7.863 \times 10^{-2} \quad (2.15)$$

or

$$\frac{E(P_o)}{P_o} = \frac{7.863 \times 10^{-2}}{P_o} + 1.778 \times 10^{-4} \quad (2.16)$$

It is seen from these equations that while the absolute error increases as P_o increases (Eq. 2.15) the relative error decreases (Eq. 2.16).

2.4 Mach-Zehnder Interferometer

The principal diagnostic tool used with the UTIAS Hypervelocity Shock Tube is a 23 cm (8") field of view Mach-Zehnder interferometer. Details of the structure and design of this particular instrument were given by Hall (Ref. 8), while many excellent reports have detailed the general theory and operation. A brief description of the apparatus will be presented here to assist in discussions of spatial resolution and alignment.

General Optics

The general configuration and principal dimensions of the interferometer are shown in Fig. 6. The interference optics consist of two beam splitters and two full-reflecting first surface mirrors, each 23 cm in diameter, arranged to give a 30° angle of incidence with respect to the central light ray. To control spacing, orientation and focussing of fringes, remote operation is provided for the rotation of mirror M_2 and splitter S_2 about two perpendicular axes in their reflecting surfaces. The translation of splitter S_1 in a direction parallel with the incoming light beam is controlled in a similar manner to enable path-length matching between the two arms of the interferometer about the central order.

The light source is collimated into parallel beams by a 25 cm diameter, 152.4 cm (60") focal-length parabolic mirror P_1 . A similar parabolic mirror P_2 serves to refocus the emergent light¹ and form a part of the camera system in focussing the object plane and interference fringes. Two small plane mirrors actually direct the light in and out of the interferometer housing.

The interferometer is placed around the shock tube with the test section located in the upper arm, and positioned to provide a Kinder arrangement in which the distances a and b shown in Fig. 6 are the same. In this way, fringe spacing and orientation may be controlled mainly by mirror M_2 with little effect on fringe focussing. A matching cylindrical compensating chamber is located in the lower arm, enclosed by two windows matching those in the test section in both dimension and tolerance. This chamber is connected to a vacuum port in the test section, 30 cm downstream of the interferometric windows, and is generally maintained at identical conditions with the test section prior to each experiment. This is not necessary, however, in view of the long coherence length of the laser light source.

Pulsed Laser Light Source

A most suitable interferometric light source, particularly for plasma studies, is a TRG, Model 104, pulsed laser system, capable of operating with lasing elements (rods) of either ruby or neodymium-doped glass by a correct choice of end reflectors. The ruby laser operates at a fundamental wavelength of 6943 Å with a spectral bandwidth of less than 0.1 Å and the neodymium laser at 10600 Å with a bandwidth of about 50 Å. In "normal-mode" operation, the lasing element is pumped by an intense burst of light from a xenon flash lamp lasting approximately 1.2 milliseconds, during which time, a series of many irregular laser pulses are emitted (providing the criteria for lasing are satisfied).

To obtain one, large short-duration pulse, the laser is Q-switched using a Pockels cell (Isomet, type 415A) electro-optic shutter and polarizer, suitably aligned in the laser cavity. The shutter is "opened" by a Baird Atomic, JM-1A high-voltage pulser which effectively removes the quarter-wave retarding voltage, applied to the Pockels cell (in this case, 3 Kv for 6943 Å), in a time less than 10 nanoseconds. In the pulser unit, a variable delay between trigger input and high voltage removal assists in accurate time control, with a synchronous monitor pulse emitted when the voltage is actually removed. As will be discussed, a disadvantage of this unit is the fact that the voltage is re-applied to the Pockels cell after a relatively long time of 1 millisecond, over which the shutter remains effectively open to some extent. For faster switching of high voltage, however, more sophisticated electronics would be necessary.

The Pockels cell shutter inhibits lasing during the flash-lamp pumping cycle until the ultimate population inversion is obtained in the laser element, at which time, ideally, the shutter should be opened to produce the most intense pulse. Since the flash-lamp radiation pulse is not ideally square, the best time appeared to be around 600 microseconds into the cycle. However, with the shutter still open, subsequent normal-mode lasing can occur if sufficient energy is still available from the flash-lamp. Consequently, an optimum time for Q-switching is required in which the large

pulse is sufficiently intense to expose the photographic plates but far enough along in the pumping cycle to prevent any significant "post-lasing" from further exposing the plates.

For the ruby laser, a time of 900 microseconds was found experimentally to be appropriate. Test measurements indicated, for this time, an output pulse width of 30 nanoseconds with a total energy of 0.8 joules using a photodiode and thermopile, respectively, implying a typical power of 24 megawatts. However, for the neodymium laser, a suitable time was not found for which the intensity was sufficient to adequately expose magnified interferograms while preventing a post-lasing blur in the flow case. Consequently, for the two-wavelength interferometry the ruby laser is adopted.

The laser is equipped with a critically oriented, KDP (potassium di-hydrogen phosphate) crystal, mounted directly at the output end of the laser cavity for second harmonic power generation. The careful alignment of this crystal with the laser is discussed by Bristow (Ref. 2), and the theory for second-harmonic generation is discussed in the literature. Power generation for this process is typically 5 to 10% efficient for the 3 cm long crystal, and produces coherent radiation at 3471.5 \AA (with a bandwidth less than 0.1 \AA) which is both parallel to and concurrent with the incident laser radiation. Consequently, by Q-switching to obtain sufficient power, the pulsed laser becomes a coherent source of two discrete wavelengths, significantly different and ideal for the method of two-wavelength interferometry.

The pulsed laser beam is focussed with a suitable condensing lens onto a circular iris, 0.8 mm in diameter, located exactly at the focal plane of the collimating parabolic mirror P_1 of the interferometer. In this manner, the ratio of light source diameter (0.08 cm) to collimating element focal length (152.4 cm) for the interferometric system is kept below 5.3×10^{-4} , corresponding to a beam divergence angle of 0.03° ($\sim 2'$). Since the distance over which the light travels through the test section is 10.16 cm, a limiting spatial resolution of the order of 0.05 mm is indicated. (Note that this is well within the boundary layer thicknesses which are typically of the order of 2 mm).

The condensing lens is chosen from simple geometry to concentrate the light source energy over the specific region of interest in any experiment as shown in Fig. 7. This was particularly important in maintaining a sufficient intensity for interferograms in which the camera magnification is increased. As shown, a suitable focal length f_c , for the condensing lens may be determined from

$$\frac{D}{d} = \frac{f_p}{f_c}$$

where d is the diameter of the pulsed laser beam, found to be 8 mm, D is the diameter of the final collimated light, and $f_p = 152.4 \text{ cm}$ is the focal length of the collimating parabolic mirror.

Consequently, a 22 cm focal-length condensing lens is adequate in illuminating a 6 cm diameter region for the boundary layer study, while a 5.3 cm focal-length lens is used when examining the entire 20 cm diameter field of view.

It is pointed out here that a condensing lens is always necessary with the high intensity laser in preventing radiation damage to the expensive optical components of the interferometer. The small input plane mirror to the interferometer was, in fact, burned occasionally because of the small beam diameter at that point, particularly with longer focal-length condensing lenses.

The advantages of the pulsed laser as a light source may be summarized as follows:

- (a) The short, 30 nanosecond light pulse is sufficiently fast to freeze the shock motion and associated phenomena.
- (b) The intensity of light at discrete wavelengths over this short duration is sufficient to expose standard photographic plates, and is much higher than the background plasma radiation.
- (c) The two discrete, significantly different wavelengths of 6943 Å and 3471 Å are suitable for the resolution of species densities in a plasma using two-wavelength interferometry.
- (d) The highly coherent, monochromatic beam ensures a long coherence length such that fringes of good contrast are visible even for relatively large mis-match in optical path lengths between the test section and compensating arms of the interferometer.
- (e) The beam is highly unidirectional and can be easily focussed down to a small size to provide excellent spatial resolution for the boundary layer studies.

Light Source Timing

Some prior knowledge of the expected shock speed (at least within 10%) is required to synchronize the pulsed laser operation with the shock-tube flow. This is necessary not only in controlling the time at which the laser is Q-switched to expose the interferogram plates, but also, prior to this, in flash-lamp pumping the lasing element for the optimum length of time. The calculations required are most easily visualized on an x-t diagram such as Fig. 4. With the time or shock position specified at which the interferogram is to be taken, the closest shock detector upstream is designated to trigger the Pockels cell, with the time difference accounted for in the high voltage pulser delay unit. Similarly, the closest shock detector at least 900 microseconds upstream is chosen to initiate the flash-lamp, with the excess time greater than 900 μsec accounted for in another delay unit.

This control of laser light source operation is included in Fig. 3. The laser flash-lamp capacitor bank is usually triggered by the shock arrival at station F, suitably delayed in a Tektronix, Type 555 Oscilloscope. The Pockels cell Q-switch is always triggered from station I, delayed correctly in the pulser delay unit, to take the interferograms at the desired time. As mentioned, the time at which the interferograms are taken is always recorded. To monitor the actual flash-lamp pumping time in each experiment, synchronization pulses from both the flash-lamp capacitor bank and the Pockels cell pulser unit are used to start and stop respectively a UTIAS

microsecond counter. It was found that variations of up to 100 μ sec in this time did not seriously affect either the quality or intensity of the interferograms, thereby allowing for some error in the actual shock speed from that predicted, for the long distance involved.

Camera System

The test-section object plane that is defined by cross-wires installed in the test model or on both windows, is focussed onto film plates or ground glass screens by the emergent parabolic mirror P_2 of the interferometer followed by one or two converging, achromatic lenses, the number depending on the desired magnification. The parabolic mirror is located approximately 206 cm from the object plane and focusses the image of the plane at a distance of 558 cm from the mirror with a corresponding magnification of 2.85. To record interferograms covering the entire 20 cm field of view, an overall magnification of 1/2 is necessary when using standard 10 cm x 13 cm (4" x 5") film plates. As shown in Fig. 7a this is accomplished by inserting an 81 cm focal-length lens, for convenience, near the focal plane of the parabolic mirror.

To obtain an image magnification of 3 (needed for boundary layer studies for example), the camera assembly is merely moved back and an additional 18 cm focal-length lens inserted, approximately 21 cm past the focussed image from the first lens as shown in Fig. 7b. The actual distance between lenses is sensitively adjusted in focussing the camera and setting the overall magnification. It should be pointed out that the lenses were selected to be physically compatible with the camera assembly and to carefully avoid laser beam focussing on any camera components.

In the camera assembly itself, simultaneous interferograms at two wavelengths are obtained using a small beam splitter and plane folding mirror, followed by respective line filters to separate the component wavelengths and shield the plates from plasma radiation. Kodak, Royal X Pan (1250 ASA), 10 cm x 13 cm plate film are used to record the interferograms. Plates are subsequently developed (7 minutes) in Kodak, DK 50 solution for best results. The mechanical shutter of the camera is opened immediately before recording, allowing the 30 nanosecond laser pulse to expose the plates. This is necessary, of course, since no mechanical shutter could react to flow changes, typically of the order of 5 mm/ μ sec.

Critical Alignment Procedures

In the two-dimensional evaluation of interferograms it is generally required that the collimated light of the interferometer test beam be perpendicular to the plane in which flow changes occur, or, in effect, parallel with the surface over which the flow travels. This condition of no changes in the light path direction enables the integrated effect of the optical path length on the interference to be resolved directly into its components of refractive index and distance. Thus, any misalignment constitutes an error in the resulting measurement. This becomes particularly important in boundary layer studies where significant flow changes occur within a region perhaps 2 mm from the flow surface, and a high degree of spatial resolution is necessary. In this case, misalignment not only causes a severe loss of accuracy but often prevents measurements otherwise possible near the surface because of surface

reflection and diffraction. Consequently, special care is taken to sensitively align the interferometer with the test model surface and optimize the spatial resolution.

As mentioned, the effective size of the laser light source was made small to maintain good spatial coherence across the field of view and thus ensure that the beam is sufficiently parallel within itself to permit a resolution of about 0.05 mm. Alignment of this test beam with the test model surface is then carried out using a procedure which ultimately made use of the spurious interference fringes which form adjacent to an extended solid surface when slight misalignment is present. This method was first proposed by Howes and Buchele (Ref. 9), and has since been used in other studies.

In view of the large physical size of the interferometer (Fig. 6), initial steps are taken in order to facilitate the alignment procedure whenever necessary. A platform was built and attached to the housing of the interferometer on which the appropriate light source could be positioned. In this manner, the light source and interferometer moved as a unit when alignment is carried out. The focal plane of the collimating parabolic mirror P_1 is then determined by first attaching a small light bulb behind a circular iris, adjustable in diameter, and directing this light into the interferometer. By aligning the input plane mirror and the parabolic mirror P_1 , and moving the iris (and light bulb), a position is found over the platform where the reflection of the light, returned from the windows of the compensating chamber, focussed directly back to the centre of the iris. The iris itself is rigidly affixed to the light source platform at this position, effectively defining a focal point of the parabolic mirror P_1 . In this manner, it is ensured that any light directed through the iris would, on reaching the parabolic mirror, form a parallel beam which would be perpendicular to the compensating chamber. It should be pointed out that this iris position was never altered again.

To align the interferometer with the shock tube bottom or the surface of the test model, a small helium-neon laser (Spectra Physics, Model 134) is mounted on the platform. By directing the laser beam through the 0.8 mm diameter iris from various angles, it is verified that the reflection of the beam from the compensating chamber windows always returned to the centre of the iris. The entire interferometer as a unit, including compensating chamber and light source, is then adjusted in both pitch and yaw with the test section of the shock tube until the reflections of the helium-neon laser beam from the test section windows are also returned to the centre of the iris. This provides a good approximation to the correct alignment with the shock tube bottom or with the surface of test models since the test section windows were very nearly perpendicular to the shock tube surfaces. A more sensitive procedure is then carried out.

To illuminate the test section, the 2 mm diameter gas laser beam is expanded by inserting a short, 1 cm focal length "eyepiece" lens in the same manner as shown in Fig. 7, such that the beam initially focussed at the iris. A moveable ground-glass screen is placed at the image plane, formed by the parabolic mirror P_2 , of the cross-wires discussed previously. The interferometer is then adjusted to focus many vertical fringes on the screen, in a desired direction. (It is pointed out that fringe spacing, etc, are controlled by mirror M_2 and splitter S_2 of the interferometer, which do not affect the incoming beam alignment with the test section.) Using a small "jeweller's" eyepiece behind the screen, the interference immediately adjacent

to the surface can then be observed at a magnification of about 20.

As predicted by Howes and Buchele (Ref. 9), spurious diagonal fringes are observed at the surface when the beam is misaligned. When the incoming beam is inclined at a small negative angle with respect to the surface these spurious fringes result from light that is reflected from the model surface (and also diffracted by the surface edge nearest the screen) and interfering with the reference beam. When the beam is at a small positive angle, diagonal fringes, oppositely inclined, resulted from the light, diffracted by the surface edge nearest the laser light source, interfering with the reference beam. When correct alignment is obtained, these spurious fringes effectively disappeared, although a slight "picket-fence" effect is observed, caused by the combination of the two opposed patterns and the diffraction pattern produced by the surface edge nearest the light source.

Consequently, while observing this interference pattern on the screen, the entire interferometer is sensitively adjusted in pitch (usually by air pressure in the pneumatic tire mounts) until the correct pattern is obtained. The final alignment is generally approached from the negative angle of the incoming beam with the surface, since the spurious fringes formed by the reflected light are more distinct than those formed by diffraction. The correct alignment with respect to yaw is also found by adjusting fringes perpendicular to the downstream surface of the test model and using the spurious fringes formed adjacent to this surface as well.

Bunting and Devoto (Ref. 10) found that the residual misalignment following this type of procedure was less than the uncertainty of the beam collimation arising from the finite size of the light source. Consequently, the limiting spatial resolution after alignment should remain as 0.05 mm.

It should be noted that, after this alignment is carried out, the reflections of the laser beam, returned from the test section windows, are found to be displaced downward from the centre of the iris by about 4 mm. This indicates from simple geometry (for the 152.4 cm focal length collimating parabolic mirror P_1) that the test section windows are about 5' of arc from being perpendicular to the flow surfaces. The position on the iris where these reflections are returned have been recorded to serve as an additional indicator as to the positioning for correct alignment.

Following this procedure, final adjustments are made to the system. The helium-neon laser is removed from the light-source platform and placed on a stand behind the platform. The narrow laser beam is again directed into the interferometer through the iris so as to pass through the centre of interest in the test section. The camera system, including lenses and film-plate holders are then positioned along the axis of this beam. Similarly, the pulsed laser light source is then mounted on the platform between the gas laser and the iris and adjusted axially with the gas laser beam. (This is easily accomplished by opening the back of the pulsed laser, allowing the beam to pass through the laser element, and aligning by means of cross-hairs at each end of the laser cavity). Final camera adjustment and focussing of fringes, etc, is done using a tungsten light placed at the iris (with the iris wide open) to more easily define the correct plane of focus. (The white light source is also used to path-length match the two arms of the interferometer to give the best fringe contrast about the central order.)

The procedures discussed in this section can be performed easily and efficiently whenever necessary, and present a marked improvement over methods previously used on this facility.

3. PRINCIPLES OF TWO-WAVELENGTH INTERFEROMETRY

The Mach-Zehnder interferometer provides a means of spatially resolving the phase refractive index throughout a two-dimensional flow field in the test section. In general, the change in refractive index from some reference condition may be determined by measuring the change in the interference pattern or "fringe shift" from this reference. Specific evaluation techniques are discussed in detail in Section 4. Using the reference-point method of analyzing interferograms as described, the change in interference is related to the change in refractive index (Eq. 4.13)

$$n(x,y) - n(x_r,y_r) = \frac{\lambda}{L} S(x,y) \quad (3.1)$$

where $S(x,y)$ is the nondimensional "fringe shift" or change in interference measured at the position (x,y) relative to the interference change at a reference point (x_r,y_r) , as defined in Section 4, Eq. 4.12,

λ is the wavelength of incident light used,

L is the width of the test section, across which the light beam travels ($10.16 \text{ cm} = 10.16 \times 10^8 \text{ Å}$ in this study)

$n(x,y)$ is the refractive index at the position (x,y) in the flow field, and $n(x_r,y_r)$ is the refractive index at the reference point (x_r,y_r) in the flow, and must be known if an absolute determination of $n(x,y)$ is to be made.

For dilute atomic or molecular gases, the phase refractive index can generally be related directly to the density by the classical Gladstone-Dale equation,

$$n-1 = K\rho \quad (3.2)$$

where

$\rho = mn$ is the gas density, which can be written in terms of particle mass m , and number density n , and

K is the Gladstone-Dale constant, which is constant for a given wavelength of light and over a large range of pressures.

The Gladstone-Dale constant may be found from the induced electric dipole polarizability of the gas, β , as (Ref. 2):

$$K = 2\pi \beta / m$$

In a dilute mixture where the interaction between constituent gases may be neglected relative to the interaction with the electric field associated with the light wave, the refractivities are additive such that

the total refractivity of the mixture is given by a summation:

$$n-1 = \sum_s (n-1)_s = \sum_s K_s \rho_s \quad (3.3)$$

where the subscript "s" refers to a species of the mixture.

Singly Ionized Plasma

As discussed by Alpher and White (Ref. 11), most plasmas may be considered in this manner, at least for incident radiation in the optical region of the spectrum. Consequently, for a singly ionized plasma consisting of a mixture of neutral atoms, ions and electrons, the total plane refractive index may be written as:

$$n-1 = (n-1)_a + (n-1)_i + (n-1)_e \quad (3.4)$$

where the subscripts a, i, e denote atoms, ions and electrons respectively. It should be noted that the neutral atom and ion components contain implicitly the contributions from the excited state as well as ground state species.

The refractivity of electrons can be obtained from the plasma dispersion formula. With no applied magnetic field, and the frequency for momentum transfer collisions between electrons and heavy particles small with respect to the frequency of the light, it may be shown that

$$(n-1)_e \approx -\frac{\omega_p^2}{2\omega^2} \quad (3.5)$$

where

$$\omega_p = \frac{4\pi n_e e^2}{m_a}$$

ω_p is the classical plasma frequency, and

m_a is the mass of atom.

$$\omega = 2\pi c/\lambda = 1.88365 \times 10^{19}/\lambda$$

ω is the angular frequency of the light source.

Finally in terms of wavelength, λ (in \AA), Eq. 3.5 becomes:

$$(n-1)_e = -\frac{4.4849 \times 10^{-14}}{m_a} \lambda^2 \quad (3.6)$$

The highly dispersive nature of the electrons is easily seen by the dependence on the square of the wavelength. The total plasma refractive index may now be written as:

$$n-1 = K_a \rho_a + K_i \rho_i - 4.4849 \times 10^{-14} \frac{\lambda^2}{m_a}$$

In a singly ionized plasma, $n_i = n_e$, $m_i \approx m_a$, and the total plasma density is given by:

$$\rho = m_a (n_a + n_e) \quad (3.7)$$

Hence, rewriting the plasma refractive index in terms of ρ and n_e :

$$n-1 = K_a \rho - \left[K_a - K_i + \frac{4.4849 \times 10^{-30}}{m_a} \lambda^2 \right] m_a n_e$$

It is convenient to define

$$Z(\lambda) = (K_a - K_i) + \frac{4.4849 \times 10^{-30}}{m_a} \lambda^2 \quad (3.8)$$

The total plasma refractive index may then be expressed as:

$$n-1 = K_a \rho - Z m_a n_e \quad (3.9)$$

The total refractive index for a singly ionized plasma is seen to depend explicitly on the plasma total density and electron number density, and implicitly on the wavelength of light through the known dispersive constants, K and Z . Consequently, if the plasma is examined interferometrically using light at two discrete wavelengths simultaneously, two values of the plasma refractive index may be found for the same plasma conditions. From Eq. (3.9), two equations in two unknowns result, and the plasma total density and electron number density can be resolved. This forms the basis for the method of two-wavelength interferometry, whose sensitivity depends on the dispersive effect of the electrons. It is important to note that no assumptions have been made to this point as to the plasma being in either thermal or chemical equilibrium.

It is most common to relate the plasma densities directly to the interference measurements, using Eq. (3.9) to replace refractive index in Eq. (3.1):

$$K_a [\rho(x,y) - \rho(x_r, y_r)] - Z m_a [n_e(x,y) - n_e(x_r, y_r)] = \frac{\lambda}{L} S(x,y) \quad (3.10)$$

In shortened notation, dropping the position coordinates and the subscript "a" from the Gladstone-Dale constant,

$$K \Delta \rho - Z m_a \Delta n_e = \frac{\lambda}{L} S$$

When two interferograms are taken simultaneously at two different wavelengths, two distinct measurements of fringe shift are made. Using subscripts "1" and "2" to denote the two wavelengths, then,

$$\begin{aligned} K_1 \Delta \rho - Z_1 \Delta n_e &= \frac{\lambda_1}{L} S_1 \\ K_2 \Delta \rho - Z_2 \Delta n_e &= \frac{\lambda_2}{L} S_2 \end{aligned}$$

where $L = 11.4 \text{ cm}$.

Solving,

$$\Delta \rho = \frac{Z_1 \lambda_2 S_2 - Z_2 \lambda_1 S_1}{L [K_2 Z_1 - K_1 Z_2]} \quad (3.11)$$

$$\Delta n_e = \frac{K_1 \lambda_2 S_2 - K_2 \lambda_1 S_1}{m_a L [K_2 Z_1 - K_1 Z_2]} \quad (3.12)$$

The constants in these equations for the two wavelengths of the previously discussed ruby laser ($\lambda_1 = 6943 \text{ Å}$, $\lambda_2 = 3471.5 \text{ Å}$) for argon and krypton are listed in Table 2.

Note that the first term in Eq. 3.8 (i.e., $K_2 - K_1$) is at least one order of magnitude smaller than the electron dispersion term, and hence, an accurate value for this ratio is not critical to the evaluation.

Diatomic Gas

For a diatomic gas Eq. (3.3) can be written in the form

$$n - 1 = (n-1)_m - (n-1)_a \quad (3.13)$$

where m designates a molecule and a an atom.

Thus Eq. 3.10 now becomes:

$$S = \frac{L}{\lambda} \left\{ \rho [K_m(1-\alpha) + K_a \alpha] - \rho_r [K_m(1-\alpha_r) + K_a \alpha_r] \right\}$$

or after rearrangement

$$S = \frac{L}{\lambda} \left\{ K_m(\rho - \rho_r) - (K_m - K_a)(\rho \alpha - \rho_r \alpha_r) \right\} \quad (3.14)$$

Following the above procedure of solving two equations (two different wavelengths) with two unknowns, $\Delta \rho$ and $\Delta(\rho \alpha)$ results in;

$$\Delta\rho = \frac{Z_1 \lambda_2 S_2 - Z_2 \lambda_1 S_1}{L(K_{m2} Z_1 - K_{m1} Z_2)} \quad (3.15)$$

$$\Delta(\rho\alpha) = \frac{K_{m1} \lambda_2 S_2 - K_{m2} \lambda_1 S_1}{L(K_{m2} Z_1 - K_{m1} Z_2)} \quad (3.16)$$

where $Z_i = K_{m_i} - K_{a_i}$ and K_{m_i} , K_{a_i} are the Gladstone-Dale constants for the molecule and the atom respectively.

It is worth noting that the final form for both singly ionized plasma (of monatomic gases) and diatomic dissociating gases is exactly identical (compare Eqs. 3.11, 3.12, 3.15 and 3.16). The constants K_{m1} , K_{a1} , K_{m2} , K_{a2} , Z_1 and Z_2 for oxygen and nitrogen are given in Table 3.

3.1 Absolute Errors

The errors in the indirect measurements of the total density, the number density the quantitative $\rho\alpha$ and ρx (α -degree of dissociation, x -degree of ionization) changes, that are directly related to the accuracy within which the fringe shifts can be measured, can be calculated using the elementary error approximation.

Total Density

Using the elementary error approximation Eqs. 3.11 and 3.15 result in:

$$E(\Delta\rho) = \pm \left\{ \left| \frac{\partial(\Delta\rho)}{\partial S_2} \right| E(S_2) + \left| \frac{\partial(\Delta\rho)}{\partial S_1} \right| E(S_1) \right\} \quad (3.17)$$

Note, $E(\phi)$ indicates the error associated with measurement " ϕ ". Thus if the errors in measuring respective fringe shifts are about the same, i.e., $E(S_1) = E(S_2) = E(S)$, Eq. 3.17 together with Eq. 3.11 or 3.15 yields

$$E(\Delta\rho) = \frac{1}{L(K_{m2} Z_1 - K_{m1} Z_2)} \left[|Z_1 \lambda_2| + |Z_2 \lambda_1| \right] E(s) \quad (3.18a)$$

for a monatomic gas, and

$$E(\Delta\rho) = \frac{1}{L(K_{m2} Z_1 - K_{m1} Z_2)} \left[|Z_1 \lambda_2| + |Z_2 \lambda_1| \right] E(S) \quad (3.18b)$$

for a diatomic gas.

Using the constants from Tables 2 and 3 for argon, krypton, oxygen and nitrogen respectively, Eqs. 3.18a and b reduce to (Note $L = 10.16$ cm):

$$E(\Delta\rho) = 4.292 \times 10^{-5} E(S) \frac{\text{g}}{\text{cm}^3} \quad \text{for argon.}$$

$$E(\Delta\rho) = 5.866 \times 10^{-5} E(S) \frac{\text{g}}{\text{cm}^3} \quad \text{for krypton}$$

$$E(\Delta\rho) = 4.031 \times 10^{-4} E(S) \frac{\text{g}}{\text{cm}^3} \quad \text{for oxygen}$$

$$E(\Delta\rho) = 2.097 \times 10^{-5} E(S) \frac{\text{g}}{\text{cm}^3} \quad \text{for nitrogen}$$

A conservative estimate of the error in measuring fringe shift is 0.05. Hence the estimated errors in the density change measurements are:

$$E(\Delta\rho) = 2.146 \times 10^{-6} \text{ g/cm}^3 \quad \text{for argon}$$

$$E(\Delta\rho) = 2.933 \times 10^{-6} \text{ g/cm}^3 \quad \text{for krypton}$$

$$E(\Delta\rho) = 2.016 \times 10^{-5} \text{ g/cm}^3 \quad \text{for oxygen}$$

$$E(\Delta\rho) = 1.049 \times 10^{-6} \text{ g/cm}^3 \quad \text{for nitrogen}$$

The Quantities $\rho\alpha$ and $\rho\chi$

The absolute errors in measuring the quantities $\rho\alpha$ or $\rho\chi$ can be written (from Eqs. 3.12 and 3.16) in the form

$$E[\Delta(\rho A)] = \pm \left\{ \left| \frac{\partial(\rho A)}{\partial S_2} \right| E(S_2) + \left| \frac{\partial(\rho A)}{\partial S_1} \right| E(S_1) \right\} \quad (3.19)$$

where A stands for either χ or α and $\rho\chi = m_a n_e$. Following the above procedure results in:

$$E[\Delta(\rho\chi)] = \frac{1}{L(K_2 Z_1 - K_1 Z_2)} \left[|K_1 \lambda_2| + |K_2 \lambda_1| \right] E(S) \quad (3.20a)$$

$$E[\Delta(\rho\alpha)] = \frac{1}{L(K_2 Z_1 - K_1 Z_2)} \left[|K_1 \lambda_2| + |K_2 \lambda_1| \right] E(S) \quad (3.20b)$$

Using the constants from Tables 2 and 3 will give:

$$E[\Delta(\rho\chi)] = 4.101 \times 10^{-6} E(S) \frac{\text{g}}{\text{cm}^3} \quad \text{for argon}$$

$$E[\Delta(\rho\chi)] = 8.408 \times 10^{-6} E(S) \frac{g}{cm^3} \quad \text{for krypton}$$

$$E[\Delta(\rho\alpha)] = 1.229 \times 10^{-2} E(S) \frac{g}{cm^3} \quad \text{for oxygen}$$

$$E[\Delta(\rho\alpha)] = 1.221 \times 10^{-3} E(S) \frac{g}{cm^3} \quad \text{for nitrogen}$$

and finally, if $E(S)$ is taken as 0.05

$$E[\Delta(\rho\chi)] = 2.051 \times 10^{-7} \frac{g}{cm^3} \quad \text{for argon}$$

$$E[\Delta(\rho\chi)] = 4.204 \times 10^{-7} \frac{g}{cm^3} \quad \text{for krypton}$$

$$E[\Delta(\rho\alpha)] = 6.145 \times 10^{-4} \frac{g}{cm^3} \quad \text{for oxygen}$$

$$E[\Delta(\rho\alpha)] = 6.105 \times 10^{-5} \frac{g}{cm^3} \quad \text{for nitrogen}$$

Number Density

By the definition of number density the following relations can be written:

$$n_e = \frac{\rho\chi}{m_a}$$

$$n_a = \frac{\rho\alpha}{m_a}$$

Thus, the absolute error in the number densities can be immediately obtained from the respective errors associated with the quantities $\rho\alpha$ and $\rho\chi$ (calculated above). Consequently, the absolute errors are;

$$\Delta(n_e) = 6.182 \times 10^{16} E(S) \frac{1}{cm^3} \quad \text{for argon}$$

$$\Delta(n_e) = 6.108 \times 10^{16} E(S) \frac{1}{cm^3} \quad \text{for krypton}$$

$$\Delta(n_a) = 4.626 \times 10^{20} E(S) \frac{1}{\text{cm}^3} \text{ for oxygen}$$

$$\Delta(n_a) = 5.249 \times 10^{19} E(S) \frac{1}{\text{cm}^3} \text{ for nitrogen}$$

Finally, if $E(S)$ is assumed to be 0.05 the absolute errors become:

$$\Delta(n_e) = 3.091 \times 10^{15} \frac{1}{\text{cm}^3} \text{ for argon}$$

$$\Delta(n_e) = 3.054 \times 10^{15} \frac{1}{\text{cm}^3} \text{ for krypton}$$

$$\Delta(n_a) = 2.313 \times 10^{19} \frac{1}{\text{cm}^3} \text{ for oxygen}$$

$$\Delta(n_a) = 2.625 \times 10^{18} \frac{1}{\text{cm}^3} \text{ for nitrogen}$$

It should be noted that all the above calculated errors have fixed values and hence, place a lower limit on the changes which can be measured.

In summary, two-wavelength interferometry provides an excellent means of measuring changes in the total density, the number density and the quantity ρX (or ρX) if the measured values are at least one order of magnitude greater than the absolute errors associated with the measurements, i.e., in the case of argon $\rho > 10^{-5} \text{ g/cm}^3$, $\rho X > 10^{-5} \text{ g/cm}^3$ and $n > 10^{16} \text{ cm}^{-3}$. The measurement technique does not perturb the gas under consideration to any appreciable extent, and may be applied equally well to nonequilibrium as well as equilibrium situations.

4. SPATIAL ANALYSIS OF INTERFEROGRAMS

In order to obtain quantitative measurements of gas densities using an interferometer, care must be taken in reducing the resulting fringe patterns correctly. As the flow being studied becomes more complex, the simpler direct evaluation methods become difficult to apply. Such an example is shown in the interferogram (Fig. 8) of the shock structure in argon near the shock tube wall. Interferograms such as these, with their dark and bright lines of interference, or fringes, contain a vast amount of information about the refractive index (and hence density) variations over the entire field of view. In order to extract the maximum amount of data in flows of any complexity, a digital evaluation program was set up for use with the 23 cm (9 in) field of view Mach-Zehnder interferometer, in which the spatial coordinates (x,y) of the various lines of interference (fringes) on the interferograms are put into digital form such that a computer analysis is then possible.

In developing the relationship between orders of interference and refractive index, the basics of interferometry are reviewed briefly as applied.

to the Mach-Zehnder interferometer whose components are shown in Fig. 9. (More details may be found in Refs. 12 and 13). Light from a coherent monochromatic source is divided by a first beam splitter S_1 , into two coherent beams, one of which travels through the test section p , while the other travels through a compensation chamber q . When reunited at the second splitter, S_2 , the light waves will interfere constructively or destructively depending on the relative time of travel through each arm. The time taken for a plane electromagnetic wave to pass through an isotropic medium may be written in terms of the "optical path length" τ as

$$\Delta t = \frac{1}{c_0} \tau$$

where c_0 is the speed of light in vacuo, and

$$\tau = \int n dl$$

where n is the refractive index, which is a function of the medium and of the frequency of the wave, and l is the geometrical path over which the wave travels, or the arc length. For coherent light, constructive interference occurs if the difference in optical path lengths between the two arms is an even multiple of half wavelengths of the light used, while destructive interference takes place if this difference is an odd multiple i.e.,

$$\int_{S_1}^{S_2} n_p dl_p - \int_{S_1}^{S_2} n_q dl_q = \begin{cases} 2N' \lambda/2 & \text{for maxima} \\ (2N' + 1) \lambda/2 & \text{for minima} \end{cases} \quad (4.1)$$

where $N' = 0, +1, +2, \dots$, may be termed the order of the interference, " p " denotes a wave travelling through the test section arm, " q " denotes a wave travelling through the compensation arm. For convenience, let the optical path lengths in the respective arms be denoted as

$$\tau_q = \int_{S_1}^{S_2} n_q dl_q$$

$$\tau_p = \int_{S_1}^{S_2} n_p dl_p = \int_{S_1}^a n_p dl_p + \int_a^b n_p dl_p + \int_b^{S_2} n_p dl_p$$

Here, the optical path length through the test section has been broken at " a ", the entrance position to the test section, and " b ", the exit position from the test section, into three additive components. The term τ^* , is then defined as:

$$\tau^* = \int_{S_1}^a n_p dl_p + \int_b^{S_2} n_p dl_p - \tau_q \quad (4.2)$$

such that τ^* accounts for all the optical path lengths outside the test section. The interference Eq. (4.1) may then be written as

$$\int_a^b n_p dl_p + \tau^* = \begin{cases} 2N' \lambda/2 & \text{for maxima} \\ (2N' + 1) \lambda/2 & \text{for minima} \end{cases}$$

To write an easier and more general relationship, a continuous linear variable, N , is considered such that:

$$\int_a^b n_p dl_p + \tau^* = N\lambda \quad (4.3)$$

where, for $N = 0, +1, +2, \dots$, there will be total constructive interference, or maxima; while for $N = +1/2, +3/2, +5/2, \dots$, there will be total destructive interference, or minima. For all other intermediate values of N , there will be varying "gray" interference, or a graduation of these two extremes.

The quantity of interest is generally the refractive index n_p of the medium in the test section, which is then related to the density^p. Thus, if the path taken by the light travelling through the test section is known, and all the optical path lengths τ^* outside the test section are accounted for, then orders of interference N measured from an interferogram may be used with Eq. (4.3) to determine the integrated or cumulative value of n_p over this path. To determine τ^* for this equation, the interference may be observed for a case where the optical path lengths in the test section are known (e.g., $n_p = \text{constant}$). This picture is referred to as the "no-flow" or reference interferogram and is denoted by the subscript "o". Then

$$\tau_o^* = N_o \lambda - \int_a^b n_{p_o} dl_{p_o}$$

where $\int_a^b n_{p_o} dl_{p_o}$

is known, and N_o is measured from the no-flow interferogram.

After the event being studied in the test section is recorded by the "flow" interferogram, τ_o^* may be used in Eq. (4.3) to find n_p , providing no changes have occurred in the optical path lengths outside the test section (i.e., $\tau^* = \tau_o^*$). However, this assumption is often subject to uncertainty, particularly if the time between the recording of the "no-flow" and "flow" interferograms is significant. A less stringent dependence on the no-flow picture can be invoked by the use of a "reference point" in the flow interferograms as described later.

Consider the coordinate system shown in Fig. 10 where the light propagation is initially in the z-direction. In the most general case, the refractive index may vary over the entire field, such that $n = n(x, y, z)$. The light path must also be such that the travel time be a minimum as given

by Fermat's principle.

$$\delta \left[\frac{1}{c_0} \int n(x,y,z) d\ell \right] = 0$$

where δ denotes the first variation of the integral.

However, to keep the analysis from becoming overly cumbersome, the following assumptions are made for a first order approximation:

1. To satisfy Fermat's principle, the refraction of light is small such that each beam may be considered to travel in a straight line path in the z-direction, perpendicular to the (x,y)-plane.
2. The refractive index n varies only across the field of view or in the (x,y)-plane, and does not vary along the beam direction z.
3. The test section windows enclosing the test chamber are exactly parallel, such that, for any (x,y)-value, the geometrical distance across the test section in the z-direction is the same value L.

The first assumption is satisfactory for many flows being examined, but becomes questionable in regions where density gradients are high. The second merely emphasizes that the interferometer is most convenient in analyzing two-dimensional flows, and becomes much more difficult to use quantitatively if changes occur in the beam direction because of the integrated effect. The third assumption is usually good, and may be pre-controlled to a known accuracy in the equipment.

Mathematically, the above stipulations translate into Eq. (4.3) in the following manner:

1. $d\ell_p = dz$
2. $n_p = n_p(x,y)$, $\tau^* = \tau^*(x,y)$
3. $b-a = L$ for all (x,y)

Hence,

$$\int_a^b n_p d\ell_p = n(x,y) L$$

and

$$n(x,y) L + \tau^*(x,y) = N(x,y) \lambda \quad (4.4)$$

Note that the order of interference N may vary across the field of view or become a function of (x,y) if the optical path lengths outside the test section and the refractive index inside the test section vary across (x,y) . Equation (4.4) makes it possible to have a digital analysis.

Some useful comments concerning the adjustment of a Mach-Zehnder interferometer will be made. In the "ideal" case with perfect optical components and coherent light, it would be possible to adjust the interferometer perfectly such that the optical lengths outside the test section do not vary over the (x,y) -plane or field of view, such that τ^* is constant, and not a function of (x,y) . Then, with constant conditions in the test section, there would be a constant interference across the (x,y) -field and hence a uniform illumination over the entire viewing screen. In other words, the screen would be totally bright, dark or gray. This adjustment leads to what is termed the "infinite fringe" method (i.e., the fringes are spaced infinitely far apart).

When changes take place in the test section during a flow, any fringes, or lines of extreme interference, which are visible will just correspond to lines of constant refractive index. This follows immediately from Eq. (4.4).

$$n(x,y) L + \tau^* = N(x,y) \lambda$$

Since $\tau^* = \text{constant}$, the orders of interference, $N(x,y)$, which are seen on the screen are directly related to the refractive index, $n(x,y)$. Along any fringe, $N(x,y) = \text{constant}$, and therefore $n(x,y)$ must be a constant. This method is often used for a qualitative examination of a flow, particularly in cases where the refractive index can be directly related to the density of the medium, as in a perfect gas. Any fringes which are visible are isopycnics or lines of constant density. However, the fringes are usually quite wide and accuracy is therefore impaired. Consequently, the infinite-fringe method is poor for quantitative measurements that require very good spatial resolution of density. Since only the extreme lines of interference (fringes) are easily detected from interferograms, the refractive index and hence density must change a sufficient amount through the flow to cause changes in optical path lengths equivalent to integer changes of wavelength. Otherwise, perhaps only one or two fringes will be visible over the entire flow from which to determine the results. In other words, the spatial resolution is generally poor. This also makes it difficult to determine the exact order of interference along the visible fringe, which is necessary in calculating the refractive index. Finally, it is almost impossible to obtain the perfect optical components to provide uniform interference over a very large area. Consequently, a fringe or two may appear only because of optical imperfections, and this effect may be difficult to account for.

These problems are overcome by using the "virtual fringe" method. In this case, one or more of the components of the interferometer are rotated slightly to produce geometrical path differences between the test section and compensating beams outside the test section. The basics of this technique are shown in Fig. 11, in which the clockwise rotation of splitter S_2 by an angle ϵ about the x -axis, produces different distances in the light path directions to where the interfering beams reunite. For positions (y,z) on the splitter above the axis of rotation, the path lengths of the test section arm are increased while those of the compensation arm are shortened, and below the axis, the opposite

is true. Looking over the (x,y) -field of view, as y increases, the path lengths in the test section arm continuously increase linearly while those in the compensation arm continuously decrease, independent of x . Therefore, with constant conditions in the test section, horizontal lines of extreme interference will appear, each successive fringe occurring at a value of y where the path length difference is again such as to produce the next minimum or maximum as shown on actual interferograms in Fig. 4a. As the angle increases, the path-length changes in the y -direction become more severe and the spacing between the fringes becomes smaller. Each successive fringe in the y -direction corresponds to the next higher order of interference, since the test section path lengths increase as y increases. Had the rotation of S_2 been in a counter-clockwise direction, the changes as a function of y would be reversed and horizontal fringes would again appear, although the orders of interference would now decrease in the y -direction. Although this very simplified description of fringe formation omits the details of focussing (Ref. 8), it should suffice for this analysis.

With available controlled rotation of the optical components about both the x and y -axes, the spacing and orientation of these "virtual" fringes can be chosen for the optimum spatial resolution of the flow being studied. The more fringes that are in the region of interest, the more locations are known at which there is identifiable interference. Consider one such location (x,y) where there is, for example, after adjustment of the interferometer, a maximum corresponding to a particular integer order of interference N' . If the refractive index in the test section then changes in the region of (x,y) , the optical path lengths will change altering the order of interference, and there will no longer be a maximum at this location. The maximum corresponding to N' will now be at some new location where the new optical path length inside the test section and the appropriate path difference outside again cause the same constructive interference. It is the measurement from an interferogram of fractional changes in fringe position which permits a sensitive determination of changes in refractive index and hence density.

In an interferogram such as Fig. 8, the lines of constant extreme interference, or fringes, along which there is total constructive or destructive interference, are easily identified. For example, each bright line corresponds to a maximum, where $N(x,y) = N'$, and N' is some integer along the line. Although the exact integer value N' , may not be known, the fringe can be assigned an arbitrary "fringe number" M' . The next bright line of interference will generally correspond to an integer value of either $N' + 1$ or $N' - 1$, depending on the direction of rotation in the initial virtual fringe adjustment. In other words, between consecutive bright fringes (or between consecutive dark fringes), $\Delta N' = \pm 1$. Hence, if this next fringe is assigned a fringe number, $M' + 1$, such that $\Delta M' = 1$, there will be a linear relationship established between the assigned fringe numbers M' , and the actual interference orders N' . In mathematical terms, if $N' = \pm \Delta M'$, then $N' = \pm M' + k$, where $k = \text{constant}$.

If the fringes have been given increasing numbers in the same direction as the actual orders of interference increase, then the plus sign prevails, while if the numbering were done in the opposite direction, the minus sign must be used. If each fringe has been assigned an integer fringe number correctly relative to the others, there will be the same different k between the true orders of interference and the assigned fringe numbers over the entire interferogram. Thus, the fringe numbers will represent the actual

orders of interference to within the unknown constant k . It should be pointed out at this stage that the major problem in analyzing complex flows from interferograms is, in fact, the correct assignment of fringe numbers over the field to represent the interference correctly. Often, fringes become difficult to follow, and extreme care must be taken. This aspect will be discussed later.

The fringe number M may be generalized to a continuous linear variable M , as was done for the interference order N , in Eq. (4.3). In this case, the centre of a fringe is taken as the location where M has the integral value of the fringe number. This corresponds to the assumption that the position of extreme interference (either total constructive or total destructive) is at the centre of the observed brightness or darkness. Then

$$N(x,y) = \pm M(x,y) + k$$

Substituting into Eq.(4.4) yields

$$n(x,y)L + \tau^*(x,y) = \pm M(x,y)\lambda + k\lambda \quad (4.6)$$

From any interferogram, $M(x,y)$ can be determined after numbering each successive fringe correctly. If the point (x,y) lies at the centre of a fringe, then $M(x,y)$ will be the integer fringe number, whereas if (x,y) lies anywhere between the centres of two bounding fringes $M(x,y)$ will be an interpolated value between the two fringe numbers. Either the dark or bright fringes may be numbered consecutively, provided that $\Delta M = 1$ between a corresponding type of fringe. For more accuracy, each bright fringe could be given an integer value and each dark fringe between given a half-integer value, although this procedure would double the work of the analysis.

The digital analysis of any interferogram involves determining $M(x,y)$ at any desired location on the picture. This procedure may be broken into three basic parts as follows.

Assignment of Fringe Numbers

The fringes over the entire interferogram are initially numbered relative to each other as correctly as possible. When beginning this process on any picture, the number assigned to the first fringe is completely arbitrary since the actual order of interference is unknown. As mentioned, however, once a particular fringe has been given a number, all other fringes must be numbered correctly relative to it in order that a constant difference k (unknown) be maintained over the entire interferogram between the selected fringe numbers and the actual orders of interference. Each interferogram will have its own value of k which can be easily handled in the subsequent analysis.

Figure 12(a) is an example of a no-flow interferogram taken with uniform conditions and hence uniform refractive index in the test section. Consecutive numbering of the dark fringes was done in a straightforward manner as shown, beginning at the entirely arbitrary value of 21. The assignment of fringe numbers for any no-flow picture is usually quite routine

unless optical imperfections are severe.

Figure 12(b) is the subsequent flow interferogram in which an ionizing shock wave in argon is travelling through the test section from right to left as it diffracts around an expansion corner. (It may be compared with Fig. 8 where vertical fringes were used to reveal different flow details.) It is important to point out that the number assigned to the first fringe in this picture is again completely arbitrary, and need have no relationship whatsoever to the no-flow interferogram. To emphasize this point, the fringe numbers have been purposely chosen different from the no-flow picture even in the pre-shock region. It is advantageous, however, to number both pictures in the same direction. The necessary criterion is only that the relative numbering between fringes on a particular interferogram be correct. In this case, some care must be taken in identifying and numbering the fringes near the wall and through the shock wave. There are more complex flows for which, in certain regions, the correct numbers may be very difficult to ascertain, and intuition or experience is necessary. However, it should be mentioned that a mistake in numbering of even one fringe will usually give physically unrealistic results. Hence, the correct integer values may become obvious from the results, and the interferogram may be easily re-analyzed with the proper fringe numbers.

Digital Storage of Fringe Coordinates

The locations of each fringe of interest over the interferogram are then recorded using a suitable "digitizer". A digitizer consists basically of a "tablet" on which a chart or picture may be secured, and a travelling cursor which may be moved at will over the tablet. The location of the cursor at any point on the tablet is displayed continuously by a digital read-out of the x and y coordinates (usually in one hundredths of an inch) with respect to the axes and origin of the tablet. These (x,y)-coordinates may be recorded through some interface such as digital tape, either continuously at a desired rate of points per second, or point by point, by depressing a "log" button with the cursor at the desired location.

The interferogram is placed on the digitizing tablet, with its (x,y)-coordinate system oriented correctly with respect to the (x,y)-axes of the tablet. This is generally accomplished by using known surfaces or cross-wire locations on the interferogram as a reference (see Figs. 8 and 12) to ensure the correct positioning and provide the necessary correspondence between the digitizer coordinate system and that used on the interferogram. After alignment has been established, the centre of each fringe is then traced over the interferogram using the digital cursor. When recording in the point mode, the cursor is moved in steps along the fringe, depressing the log button at each step to record the (x,y)-coordinate. In the continuous mode, the log button is held depressed and the recording of coordinates is done automatically at a pre-selected number per second as the cursor is moved continuously along the fringe. The two recording modes are used interchangeably with continuous recording in regions where the fringe is smooth, and a more careful point by point recording where rapid variations occur. In either mode, the recorded points must be sufficiently close for the subsequent analysis such that the fringe location between any two points can be accurately given by a joining straight line. Consequently, when digitizing has been completed, a sufficient number of points will have been digitized (recorded) to accurately define the location of each fringe

anywhere over the interferogram.

An example of the results of this procedure is shown in Fig. 13. In this case, the dark fringes, digitized from the interferogram in Fig. 12(b) have been replotted using an IBM 1627 Calcomp Digital Plotter connected with an IBM 1130 computing system. Each fringe, of course is actually described by a number of recorded, discrete points as shown at the top of the figure for a particular fringe number. In the full plot, the plotter pen has merely been left down as it travelled from point to point along each fringe. As can be seen, it is an accurate representation of the interferogram, and the data is now in digital form suitable for analysis.

Determination of $M(x,y)$

The value of M at any desired location (x,y) is necessary if Eq. (4.6) is to be used to find the refractive index at that point. Since many points across the interferogram have been recorded by the digitizing procedure at which integer values of M (fringe numbers) are known, a two-dimensional interpolation scheme would seem appropriate, if not somewhat lengthy, in finding M at other positions. However, if the position of each fringe can be determined accurately, even between the discrete points by linear interpolation (straight-line segments) as specified above, the problem remains only in finding $M(x,y)$ at off-fringe locations. Restating this, since lines can be defined from the digitizing procedure along which M is known, all that remains is to determine M at positions not on the lines. This is accomplished in the following manner.

The interferogram is divided into a grid of constant "argument" lines, as closely spaced as desired and generally perpendicular to the average direction of the no-flow fringes. The most convenient choice of argument lines (although not a necessity) for data handling are lines along which one coordinate remains constant. For example, with basically horizontal fringes as in Fig. 13 a grid of lines of constant " x " is generated as shown in Fig. 14(a). For vertical fringes, a grid of lines of constant y would be most suitable. From the digitized data, the intersection points of any fringes with an argument line can be found. Thus, for each argument line, a plot may be made of fringe number versus the coordinate of intersection. The quantity M may then be found at any coordinate along the argument line by a one-dimensional interpolation. As a result, to find M at any location (x,y) , the correct argument line passing through the point is chosen, along with discrete values of M are known, and a one-dimensional interpolation is done along the line to find M at this point.

The procedure is demonstrated in Figs. 14(a) and (b) where the grid consists of lines $x_i = \text{constant}$. For each argument line a plot may be of the variation of fringe number M with y as shown in Fig. 14(b). An interpolation of chosen order may be done to determine M at any specific value of y . This process is handled easily by a computer and may be performed quickly and often.

With a method available for determining $M(x,y)$ as desired from any interferogram, the use of Eq. (4.6) will now be examined in more detail. After the interferometer has been suitably aligned with the desired number and spacing of virtual fringes, a no-flow interferogram is taken where the refractive index in the test section has a known and uniform value,

$$n(x,y) = n_0 = \text{constant}$$

Then

$$n_0 L + \tau_0^*(x,y) = \pm M_0(x,y)\lambda + k_0\lambda \quad (4.7)$$

where again, the subscript 0 denotes the no-flow picture. Although n_0 is known and $M_0(x,y)$ can be determined from the interferogram, k_0 the constant difference between the fringe numbering and the real orders of interference is not known.

For the subsequent interferogram taken of the flow under study, Eq. (4.6) will be simply restated:

$$n(x,y)L + \tau^*(x,y) = \pm M(x,y)\lambda + k\lambda$$

It is advantageous that the fringe numbering in the flow picture be in the same direction as the no-flow picture, such that the same sign holds in both expressions. Subtracting

$$[n(x,y) - n_0] L + [\tau^*(x,y) - \tau_0^*(x,y)] = \pm [M(x,y) - M_0(x,y)]\lambda + (k - k_0)\lambda \quad (4.8)$$

If no changes have taken place outside the test section during the time when the two interferograms are taken, then $\tau^*(x,y) = \tau_0^*(x,y)$. Moreover, since n_0 is known, and $M(x,y)$ and $M_0(x,y)$ may be measured from the respective interferograms, it is then possible to determine the refractive index in the flow $n(x,y)$, to within the constant, $(k - k_0)$, i.e.,

$$[n(x,y) - n_0] L = \pm [M(x,y) - M_0(x,y)]\lambda + (k - k_0)\lambda \quad (4.9)$$

If the difference between the chosen fringe numbering and the actual orders of interference happens to be the same in both pictures, then $k = k_0$, and the calculations may be made directly. If not, it is known that $(k - k_0)$ must be an integer, and it is not difficult in most cases to find its value from the results since an incorrect choice usually gives unrealistic answers.

However, it is found from practical experience that the assumption of no change in optical path lengths outside the test section between the no-flow and flow interferograms is often incorrect. This usually arises from the inability to control the outside conditions absolutely. Small temperature changes (and hence density) and minute physical movements of the optical components, caused either thermally or otherwise, are difficult to avoid. Because of this, a stronger method is often used which requires that a reference point exist somewhere on the flow interferogram at which the refractive index is known. The use of this reference point can at least accommodate uniform changes in $\tau^*(x,y)$ between no-flow and flow pictures and

eliminates the necessity of choosing the correct value for $(k-k_0)$.

Denoting the coordinates of this reference point as (x_r, y_r) , Eq. (4.8) must be satisfied at this particular location since it is valid for any point on the interferogram.

$$[n(x_r, y_r) - n_0]L + [\tau^*(x_r, y_r) - \tau_0^*(x_r, y_r)] = \pm [M(x_r, y_r) - M_0(x_r, y_r)]\lambda + (k-k_0)\lambda$$

Subtracting this expression from the general Eq. (4.8) for all point

$$\begin{aligned} [n(x, y) - n(x_r, y_r)]L + [\tau^*(x, y) - \tau_0^*(x, y)] - [\tau^*(x_r, y_r) - \tau_0^*(x_r, y_r)] \\ = \pm \{ [M(x, y) - M_0(x, y)] - [M(x_r, y_r) - M_0(x_r, y_r)] \} \lambda \end{aligned} \quad (4.10)$$

If the changes which take place in $\tau^*(x, y)$ during the time the no-flow and flow pictures are taken are uniform for all (x, y) , then

$$\tau^*(x, y) - \tau_0^*(x, y) = \tau^*(x_r, y_r) - \tau_0^*(x_r, y_r)$$

(It should be noted here that it is almost impossible to account for changes which might take place outside the test section which vary across the field of view.) Equation (4.10) then reduces to:

$$[n(x, y) - n(x_r, y_r)] \frac{L}{\lambda} = \{ [M(x, y) - M_0(x, y)] - [M(x_r, y_r) - M_0(x_r, y_r)] \} \quad (4.11)$$

Therefore, using some reference point (x_r, y_r) :

- (a) $n(x_r, y_r)$ must be known, but
- (b) $k-k_0$ need not be known,
- (c) n_0 need not be known.

The term $M(x_r, y_r) - M_0(x_r, y_r)$ is a particular value determined from the interferograms. It not only accounts for the refractive index change in the test section at the particular point (x_r, y_r) but also for:

- (a) The fringe numbering difference between the no-flow and flow pictures, and
- (b) any uniform changes occurring outside the test section during the time the two pictures are taken.

This is easily seen if the reference point can be chosen in a region where conditions in the test section have not changed between the no-flow and flow pictures, as in the region ahead of the shock wave in Fig. 12(b). Then, any non-zero value of $M(x_r, y_r) - M_o(x_r, y_r)$ must be due to either the choice of fringe numbering made in each picture, or to changes outside the test section.

The right-hand side of Eq. (4.11) is termed the fringe shift S which compares the observed change in interference at the point (x, y) between the no-flow and flow interferograms to that at a reference point (x_r, y_r) .

$$S(x, y) = \pm \{ [M(x, y) - M_o(x, y)] - [M(x_r, y_r) - M_o(x_r, y_r)] \} \quad (4.12)$$

As discussed previously, the choice of sign depends on the initial virtual fringe adjustment of the interferometer. If the fringe numbers have been arbitrarily chosen to increase in the same direction as the actual orders of interference increase, the plus sign holds, whereas, if the numbering were done in the opposite direction, the minus sign must be used. If the incorrect choice of sign is made, all fringe shift values will be opposite in sign from reality, and the calculated refractive index will then vary from the reference value in the reverse manner. Often, negative values of $n(x, y)$ result, easily identifying the mistake. In almost all cases, there is some region in the picture where it is known that the density and hence refractive index either increases or decreases, such as through a shock wave, compression wave, expansion wave, contact surface, slipstream and boundary layer. Consequently, the correct sign, which holds over the entire interferogram, can be easily confirmed or corrected from a brief look at results, and presents no problem in the analysis.

In summary, the usual fringe shift equation for interferometry may be written from Eq. (4.12) as:

$$S(x, y) = \frac{L}{\lambda} [n(x, y) - n(x_r, y_r)] \quad (4.13)$$

where

$$S(x, y) = \pm \{ [M(x, y) - M_o(x, y)] - [M(x_r, y_r) - M_o(x_r, y_r)] \}$$

Using a digital analysis technique, M_o and M may be determined from the respective no-flow and flow interferograms at any location (x, y) , including (x_r, y_r) thereby allowing a calculation of S . Therefore, knowing L, λ , and $n(x_r, y_r)$ enables a final determination of refractive index, n , at any

location (x,y).

5. CONCLUSIONS

The experimental techniques associated with the UTIAS 10 cm x 18 cm Hypervelocity Shock Tube were described. The inaccuracy involved in the measurements of the initial pressure P_0 , initial temperature T_0 , incident shock-wave Mach number M_s and the density ρ at any point of a given interferogram were calculated.

A new computerized method for evaluating complex flow interferograms was presented. The present method has the following advantages over previous techniques:

- 1) It can easily handle complex-flow fields.
- 2) It can account for the changes in the optical path length that occur outside the test section during the time interval taken to record the "no-flow" and "flow" interferograms.
- 3) Once the interferograms are digitized, corrected and stored on a computer disk, the total density, electron-number density and degree of ionization profiles can be obtained along any predetermined line within several minutes.

One outstanding problem, which would reduce the evaluation even further, is to develop a totally automated-computerized method of evaluating interferograms rather than the semi-computerized (hand digitized) method presented here. Undoubtedly, such a solution would evolve if more experimenters made more use of interferometry for investigating complex flows. However, the correct assignment of fringe number over the field of view, to represent correctly the interference order, would probably still be done manually.

REFERENCES

1. Boyer, A.G. "Design, Instrumentation and Performance of the 4 x 7 inch Shock Tube", UTIAS Report No. 99 (1965).
2. Bristow, M. "An Experimental Determination of the Polarizability for Single Ionized Argon", UTIAS Report No. 158 (1971).
3. Benoit, A. "Thermodynamic and Composition Data for Constant Volume Combustion of Stoichiometric Mixtures of Hydrogen-Oxygen Diluted with Helium and Hydrogen", UTIAS Technical Note No. 85, (1964).
4. Glass, I.I.
Hall, J.G. Handbook of Supersonic Aerodynamics, Section 18, Shock Tubes, NAVORD Report 1488, (Vol.6), Bureau of Naval Weapons (1959).
5. Tang, F.C. "Effects of Impurities on Shock Wave Stability and Structure in Ionizing Monatomic Gases", UTIAS Technical Note No.212, (1977).
6. Higashimo, F.
Oshima, N. "Real Gas Effects on Converging Shock Waves", Astronautica Acta, Vol. 15 (1970).
7. Russell, D.A. "Shock Wave Strengthening by Area Convergence", J. of Fluid Mech. Vol. 27, Part 2 (1967).
8. Hall, J.G. "The Design and Performance of a 9 inch Plate Mach-Zehnder Interferometer", UTIAS Report No. 27 (1954).
9. Howes, W.L.
Buchelee, D.R. "Practical Considerations in Specific Applications of Gas-Flow Interferometry", NACA TN 3507, (1955).
10. Bunting, J.O.
Deveto, R.S. "Shock Tube Study of Thermal Conductivity of Argon", Stanford University, Dept. of Aeronautics & Astronautics, SUDAAR No. 313 (1967).
11. Alpher, R.A.
White, D.R. "Optical Refractivity of High-Temperature Gases. I: Effects Resulting from Dissociation of Diatomic Gases," The Physics of Fluids, No.2, Vol.2, (1959). "Optical Refractivity of High-Temperature Gases. II: Effects Resulting from Ionizing of Monatomic Gases", The Phys. of Fluids, No.2, Vol.2, (1959).
12. Ladenburg, R.
Bershafer, D. "Physical Measurements in Gas Dynamics and Combustion", Article A3, Princeton University Press, (1954).
13. Eckert, E.R.G.
Goldstein, R.J. "Measurements in Heat Transfer", Chap. 5, McGraw-Hill, (1967).

TABLE 1: INITIAL CONDITIONS FOR NON-COMBUSTION RUNS

M_s	P_{41}	Driving Gas
Test Gas - Oxygen		
1.9	40	O ₂
2.1	80	O ₂
2.5	270	O ₂
2.8	660	O ₂
3.5	130	He
4.2	230	He
4.9	670	He
5.7	1610	He
7.2	930	H ₂
7.8	1610	H ₂
Test Gas - Nitrogen		
2.0	110	CO ₂
3.7	220	H ₂
4.8	690	He
6.2	800	He
7.0	1550	H ₂
7.8	3320	H ₂
Test Gas - Argon		
2.0	60	CO ₂
3.0	70	He ²
4.4	350	He
5.2	800	He
6.1	520	H ₂
6.9	1000	H ₂
7.9	1900	H ₂

The thickness of the mylar diaphragm is calculated from Eq. 1.1

TABLE 2: GLADSTONE-DALE CONSTANTS FOR ARGON AND KRYPTON

constant gas	K_1	K_2	Z_1	Z_2
Argon ($K_I = 0.65 K_A$)	0.1574	0.1629	3.314	0.8718
Krypton ($K_I = 0.75 K_A$)	0.1127	0.1188	1.599	0.4244

1) $\lambda_1 = 6943 \text{ \AA}$

2) $\lambda_2 = 3471.5 \text{ \AA}$

K_1, K_2, Z_1 and Z_2 are all in cm^3/g .

TABLE 3: GLADSTONE-DALE CONSTANTS FOR OXYGEN AND NITROGEN

constant gas	K_{m1}	K_{a1}	K_{m2}	K_{a2}	Z_1	Z_2
Oxygen	0.1907	0.185 $\pm 1\%$	0.1988	0.192 $\pm 1\%$	0.0057	0.0068
Nitrogen	0.2376 $\pm 0.03\%$	0.328 $\pm 1.7\%$	0.246 $\pm 0.03\%$	0.331 $\pm 2.5\%$	-0.0904	-0.0805

1) $\lambda_1 = 6943 \text{ \AA}$

2) $\lambda_2 = 3471.5 \text{ \AA}$

$K_{m1}, K_{a1}, K_{m2}, K_{a2}, Z_1$ and Z_2 are all in cm^3/g .

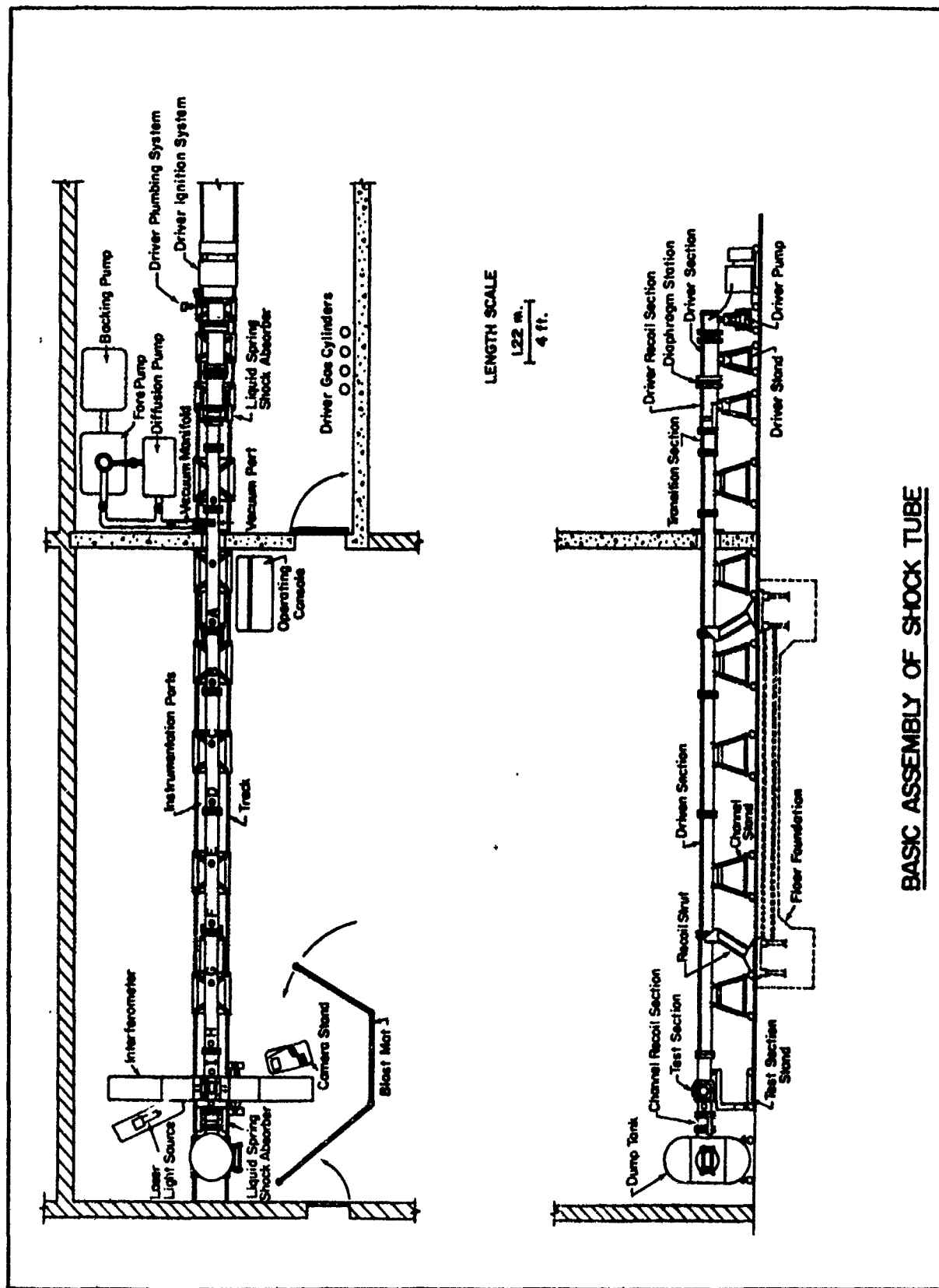


FIG. 1 GENERAL TOP AND SIDE VIEW OF THE UTIAS 10 CM X 18 CM HYPERVELOCITY SHOCK TUBE.

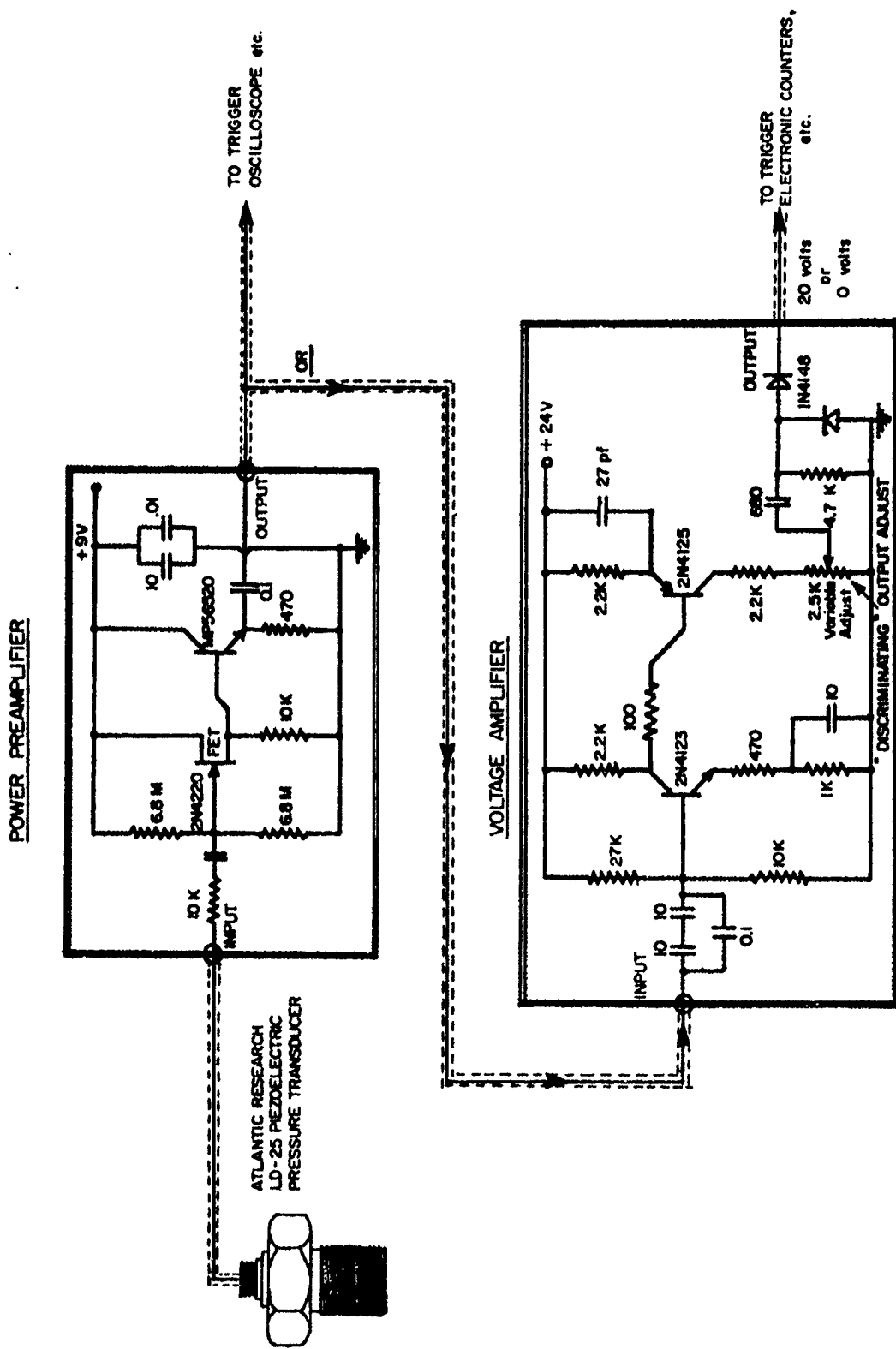


FIG. 2 SCHEMATIC DIAGRAM OF THE ELECTRONIC CIRCUITS OF THE SHOCK DETECTION EQUIPMENT.

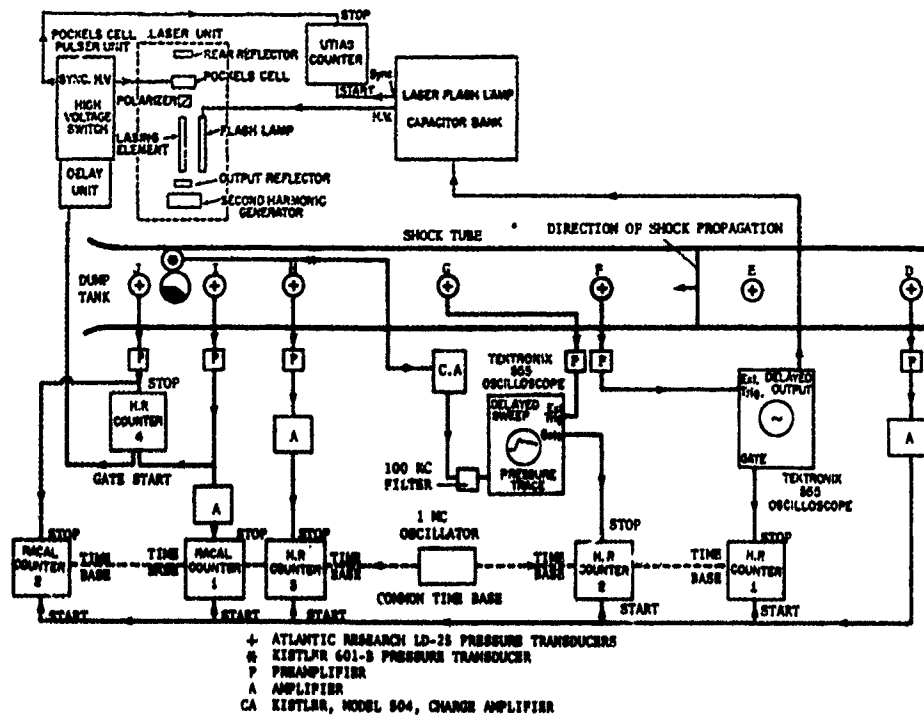


FIG. 3 INSTRUMENTATION SET-UP FOR RECORDING THE NON-STATIONARY PHENOMENA IN THE TEST SECTION.

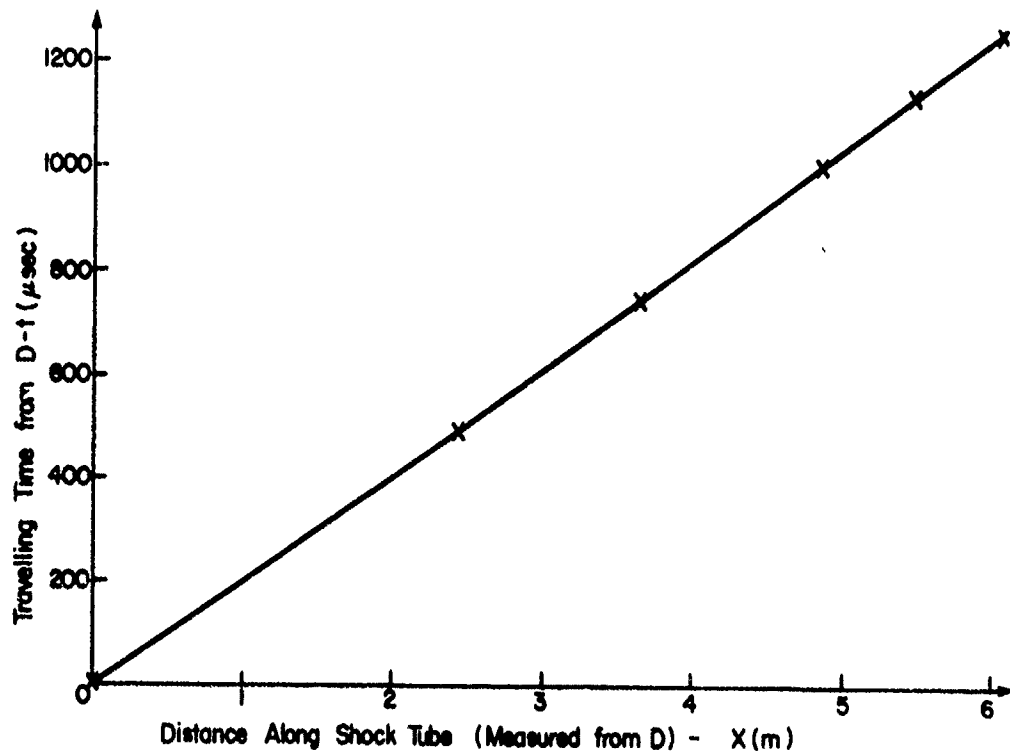
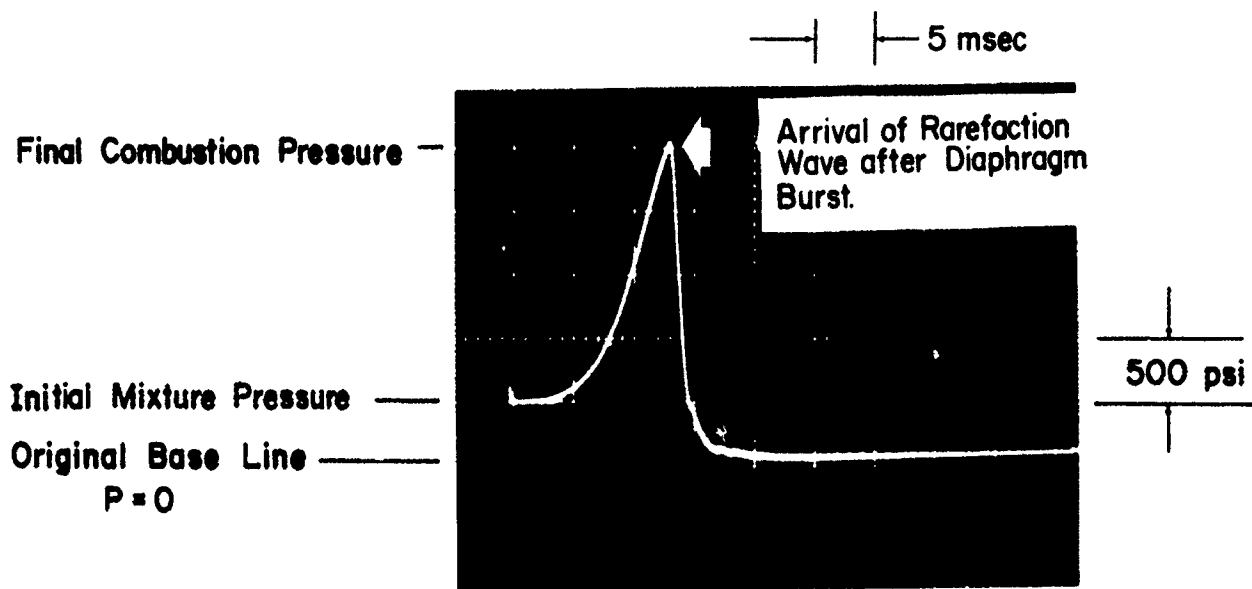


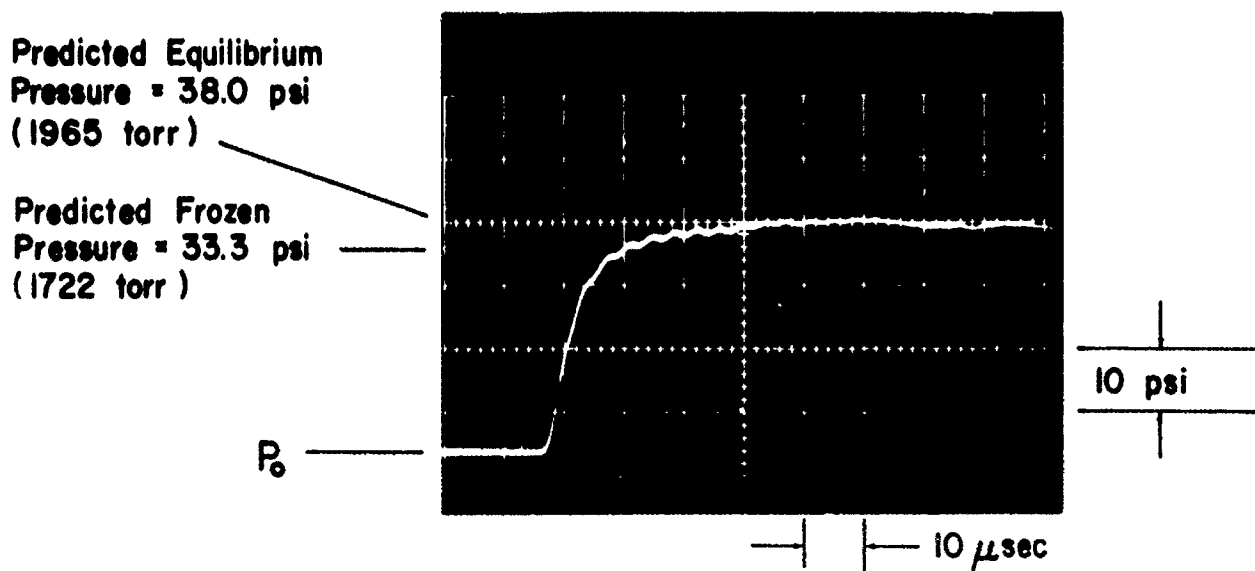
FIG. 4 DISTANCE-TIME DIAGRAM OF THE INCIDENT SHOCK-WAVE AS IT MOVES ALONG THE SHOCK TUBE. TIMES ARE MEASURED FROM D (see Fig. 3). THE SIX POINTS CORRESPOND TO STATIONS D, F, G, H, I AND J OF FIG. 3. THE SOLID LINE REPRESENTS THE BEST FIT ACROSS THESE MEASUREMENTS. THE VELOCITY OF THE INCIDENT SHOCK-WAVE AT ANY POINT IS $\frac{dx}{dt}$.

Measured Initial Mixture Pressure (H_2, O_2, He) = 423 psi (Heise Gauge)
 Calculated Diaphragm Bursting Pressure = 2452 psi



a) DRIVER PRESSURE at CLOSED END

Measured Shock Mach Number = 15.0 at Station M
 Measured Initial Pressure P_0 = 6.12 torr (0.12 psi)



b) SHOCK - WAVE PRESSURE at STATION M

FIG. 5 TYPICAL PRESSURE HISTORIES AT THE TEST SECTION (a) AND THE BACK END OF THE DRIVER SECTION (b).

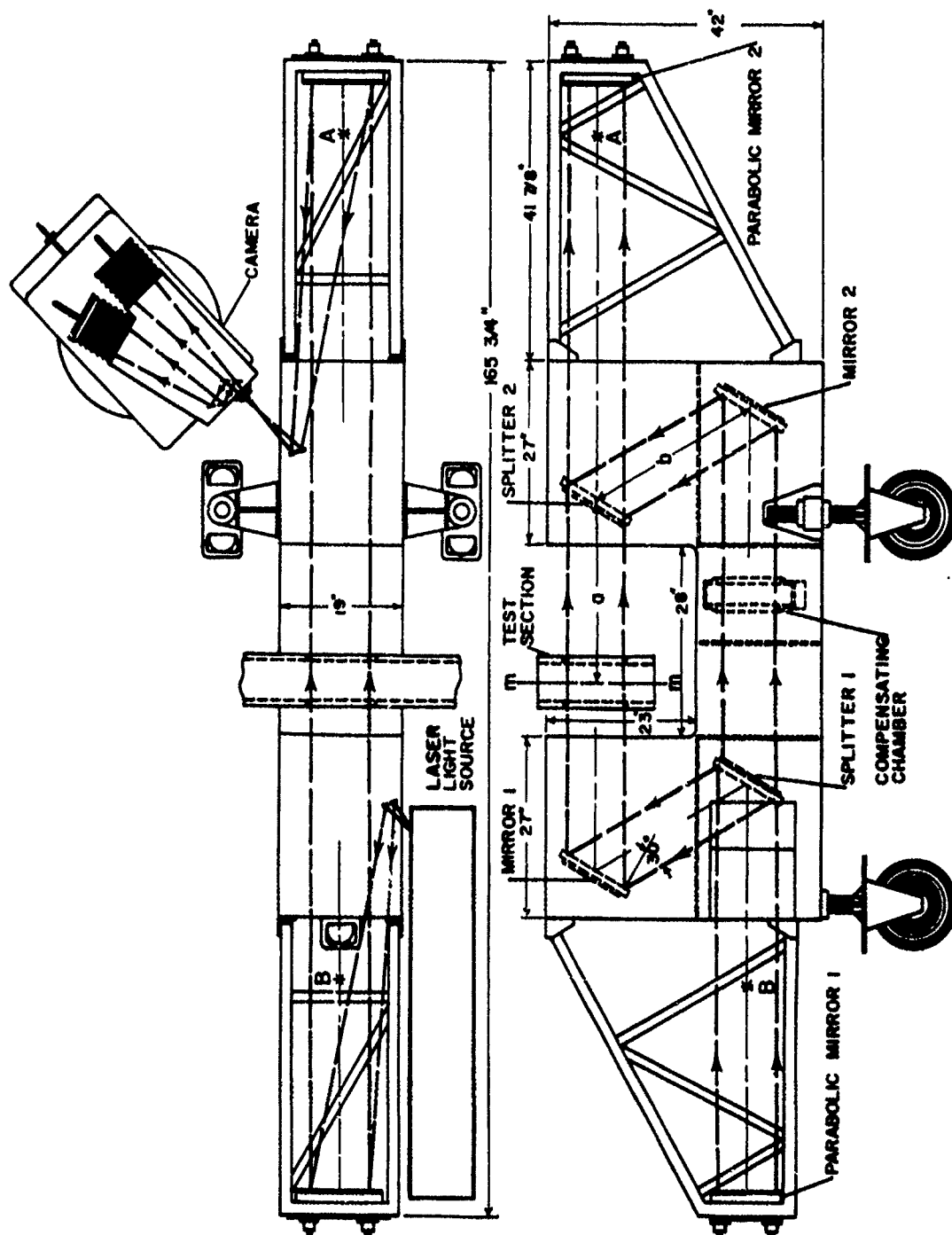
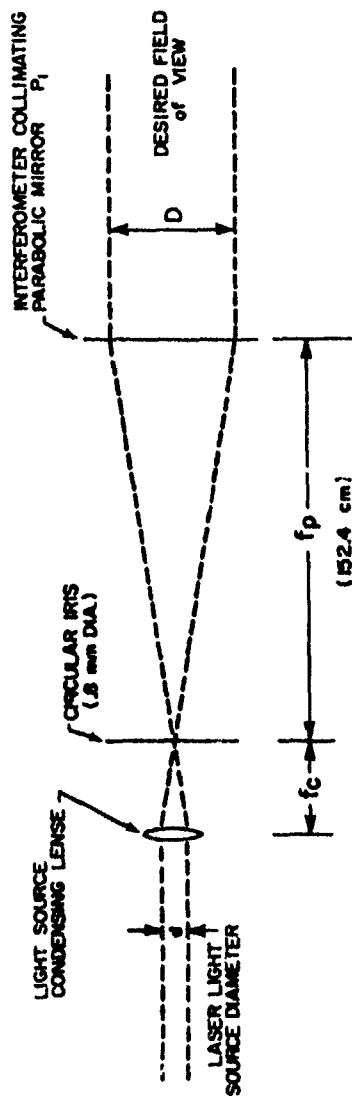


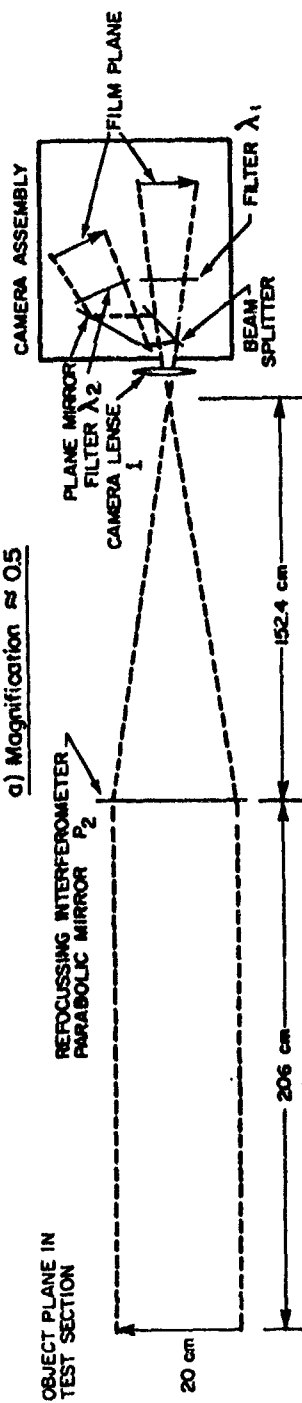
FIG. 6 SCHEMATIC OF MACH-ZEHNDER INTERFEROMETER.

LIGHT SOURCE OPTICS



CAMERA OPTICS

a) Magnification ≈ 0.5



b) Magnification ≈ 3.0

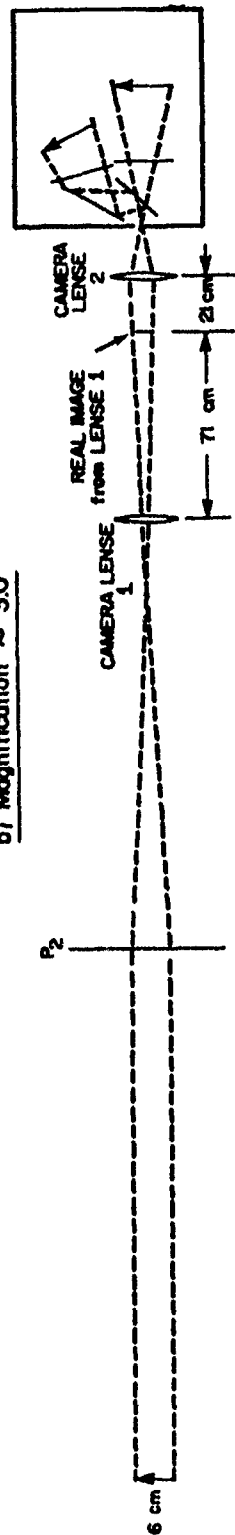


FIG. 7 SCHEMATIC DIAGRAM OF THE LIGHT SOURCE AND CAMERA OPTICS FOR OVERALL MAGNIFICATIONS OF (a) 0.5 AND (b) 3.0.

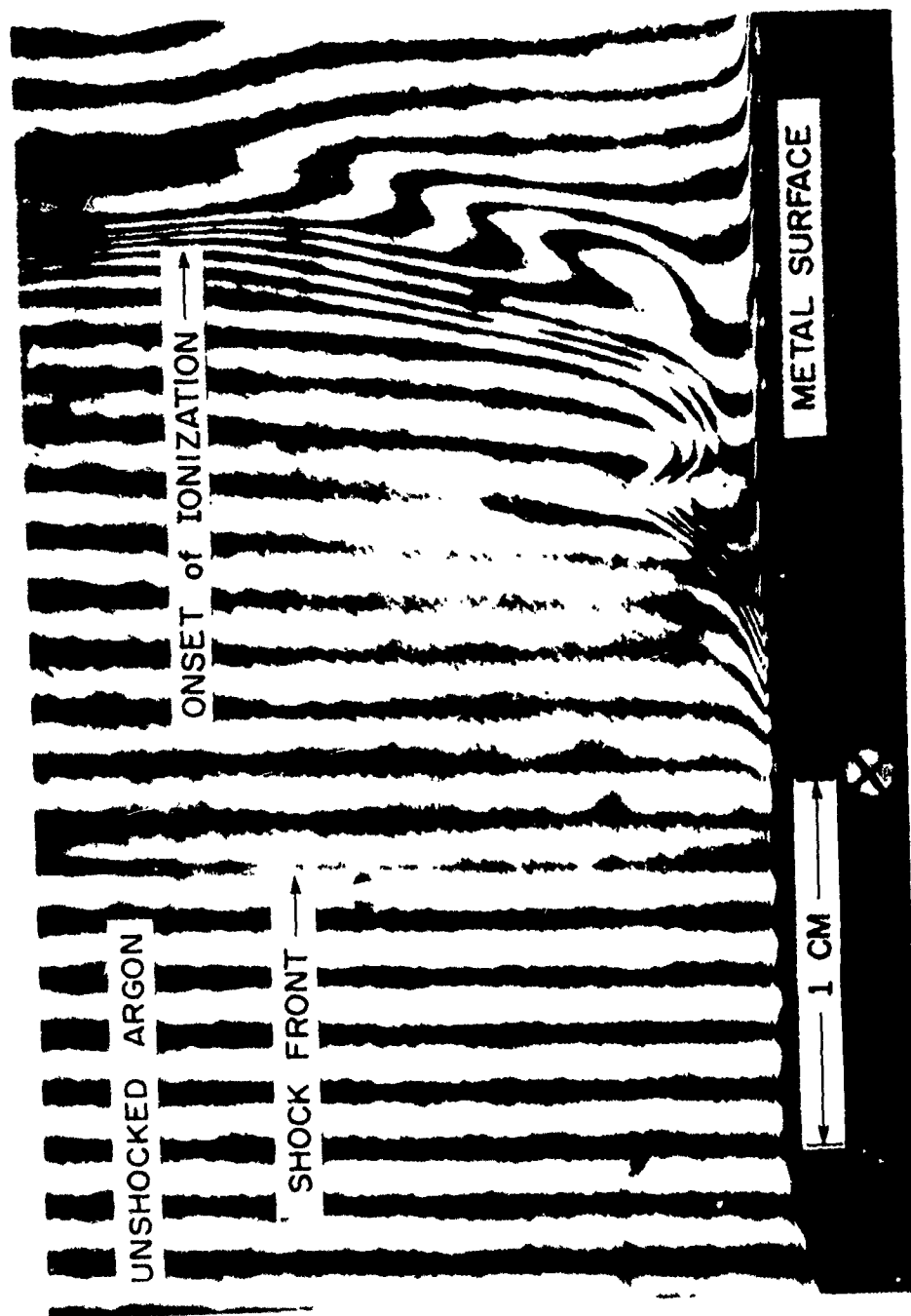


FIG. 8 INTERFEROGRAM OF NON-STATIONARY SHOCK-WAVE STRUCTURE IN ARGON NEAR THE SHOCK TUBE WALL (DISTANCE BETWEEN REFERENCE CROSS-WIRES IS 1 CM). INCIDENT SHOCK-WAVE MACH NUMBER $M_1 = 15.9$, LIGHT SOURCE WAVELENGTH $\lambda = 6943\text{\AA}$ (SHOCK-WAVE IS TRAVELLING FROM RIGHT TO LEFT).

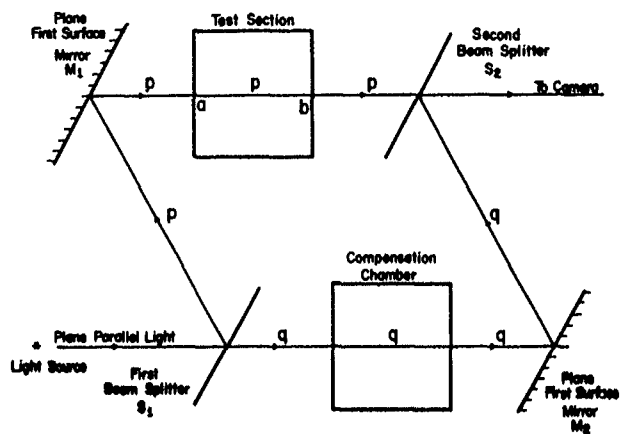


FIG. 9 BASIC COMPONENTS OF A MACH-ZEHNDER INTERFEROMETER.

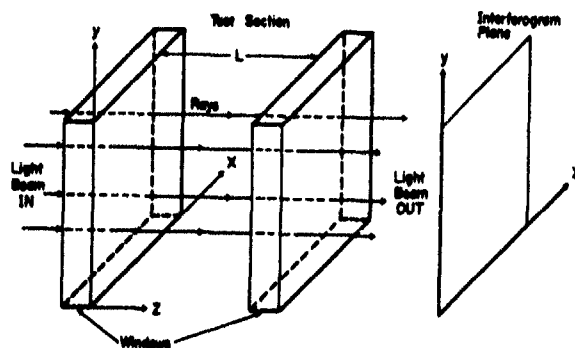


FIG. 10 COORDINATE SYSTEM USED FOR INTERFEROMETRIC ANALYSIS.

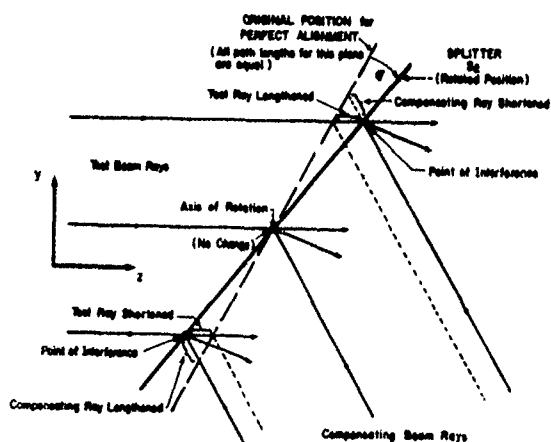
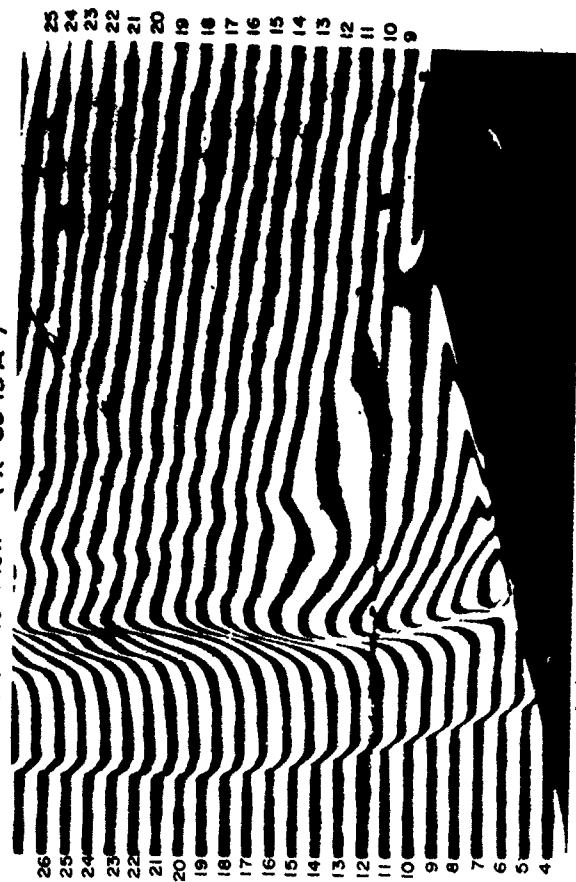


FIG. 11 'VIRTUAL' FRINGE CREATED IN THE PLANE OF SPLITTER S_2 .



(a) No Flow ($\lambda = 6943 \text{ \AA}$)



(b) Flow ($\lambda = 6943 \text{ \AA}$)

FIG. 12 DIFFRACTION AROUND AN EXPANSION CORNER OF AN IONIZING SHOCK-WAVE IN ARGON (SHOCK-WAVE IS TRAVELLING FROM RIGHT TO LEFT)
S - TRANSLATIONAL SHOCK FRONT, E - ELECTRON CASCADE FRONT, SE - IONIZATION RELAXATION DISTANCE.
(a) NO-FLOW INTERFEROGRAM ($\lambda = 6943 \text{ \AA}$)
(b) FLOW-INTERFEROGRAM ($\lambda = 6943 \text{ \AA}$)

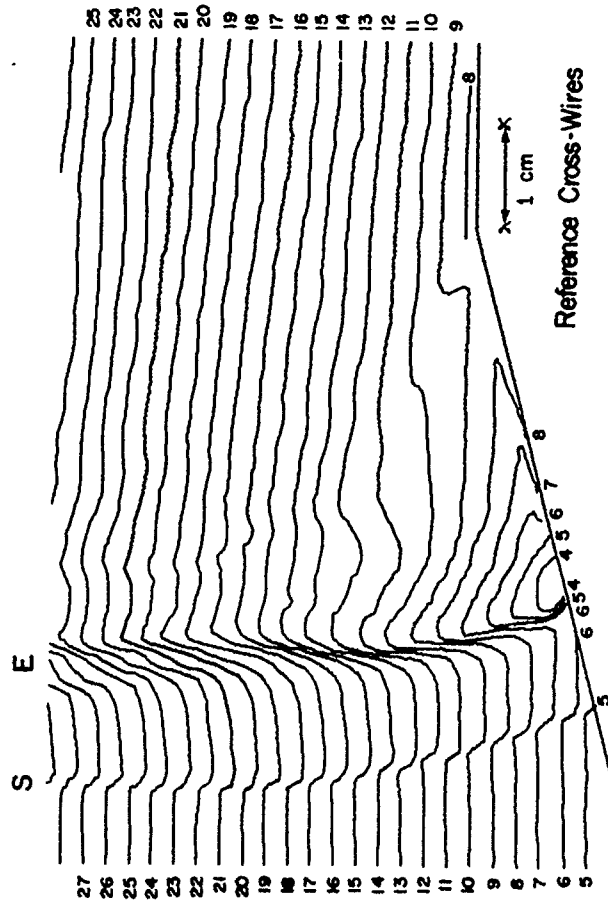
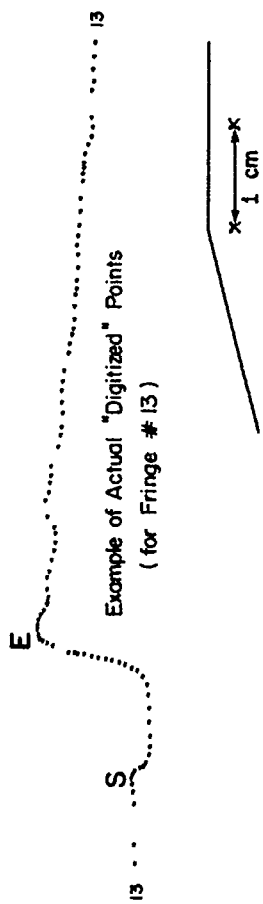


FIG. 13 DIGITIZED VERSION OF THE INTERFEROGRAM SHOWN IN FIG. 12(b).

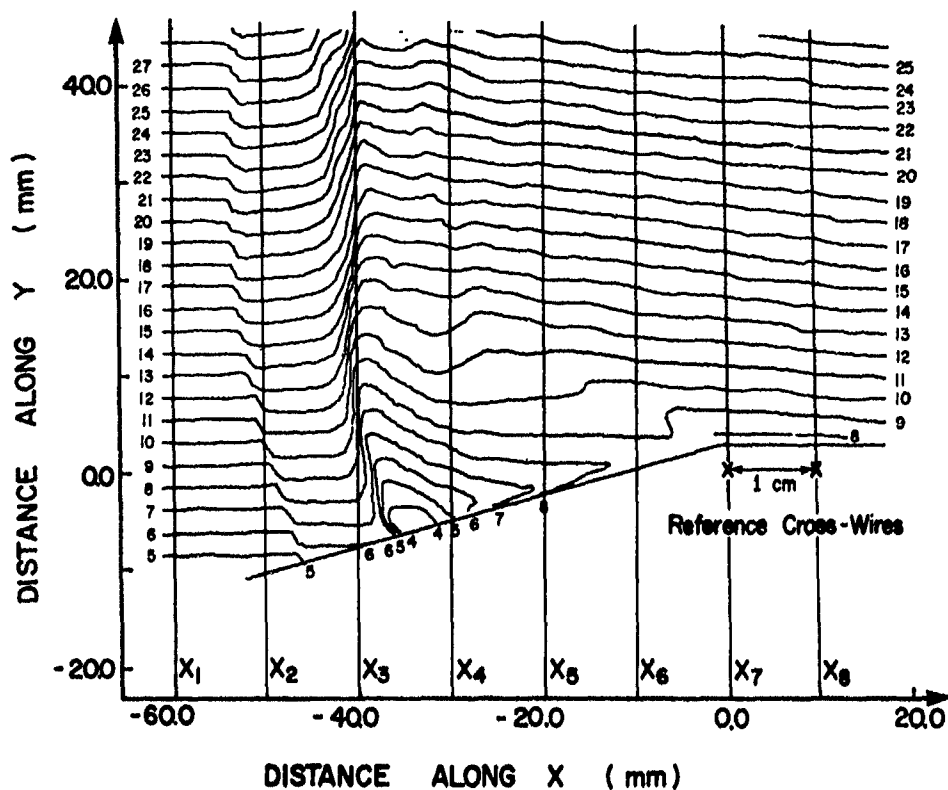
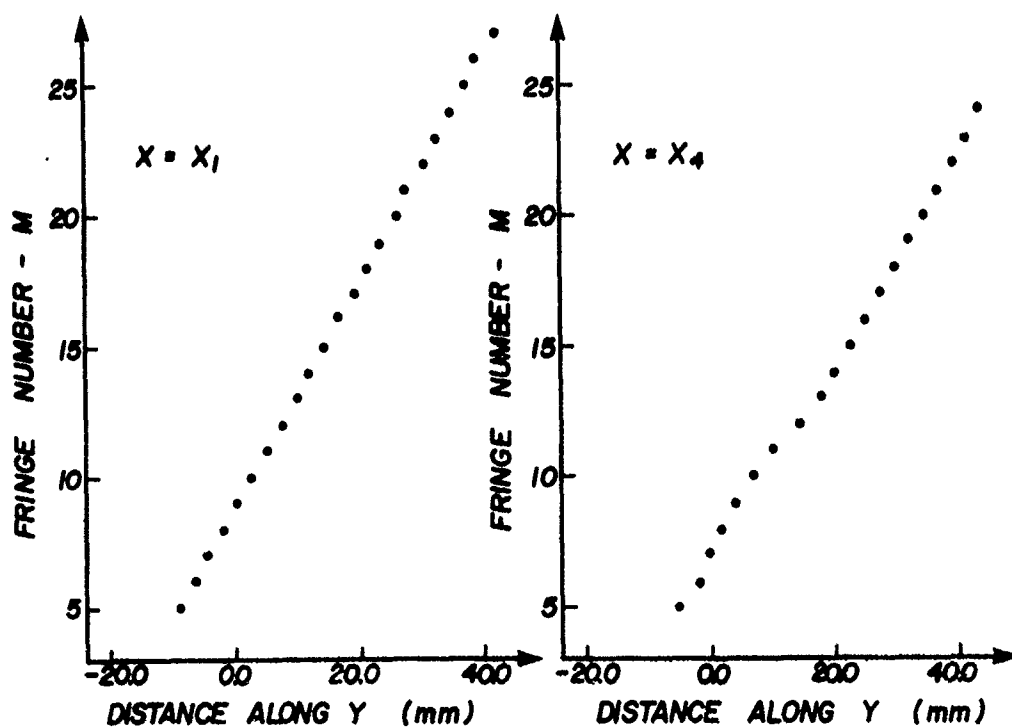


FIG. 14 (a) SUPERPOSITION OF ARGUMENT LINES $x_i = \text{CONSTANT}$ ON DIGITIZED INTERFEROGRAMS. (NOTE IN AN ACTUAL ANALYSIS THE GRID LINES WOULD BE MUCH MORE CLOSELY SPACED).



(b) PLOTS OF FRINGE NUMBER M VERSUS FRINGE POSITION y ALONG ARGUMENT LINES x_i .

UTIAS Technical Note No. 208

Institute for Aerospace Studies, University of Toronto (UTIAS)
4925 Dufferin Street, Downsview, Ontario, Canada, M3H 5T6

INTERFEROMETRIC TECHNIQUES AND DATA EVALUATION METHODS
FOR THE UTIAS 10 cm x 18 cm HYPERVELOCITY SHOCK TUBE

Ben-Dor, G., Whitten, B. T. Approx. 60 pages 14 figures 3 tables

1. Interferometry 2. Shock tubes 3. Measurement error analysis

I. Ben-Dor, G., Whitten, B. T. II. UTIAS Technical Note No. 208

The UTIAS 10 cm x 18 cm Hypervelocity Shock-Tube has been used in recent years to study ionizing shock structures, flat-plate and sidewall boundary layers and nonstationary oblique shock-wave diffractions over compression corners. These phenomena were recorded using a 23-cm dia. field of view Mach-Zehnder interferometer equipped with a giant pulse dual-frequency ruby laser.

In order to extract the maximum amount of data in these complex flows a digital evaluation method was employed. For this technique a new approach to the theory of interference was developed. In this approach the spatial coordinates (x,y) of the various lines of interference (fringes) on the interferograms are put into digital form, thereby making a computer analysis possible.

The experimental technique and instrumentation associated with the various measurements involved in research using the UTIAS 10 cm x 18 cm Hypervelocity Shock-Tube are described. Finally, the maximum possible absolute and relative errors associated with these measurements are calculated for four different gases (argon, krypton, oxygen and nitrogen) which are usually used as test gases.

Available copies of this report are limited. Return this card to UTIAS, if you require a copy.



UTIAS Technical Note No. 208

Institute for Aerospace Studies, University of Toronto (UTIAS)
4925 Dufferin Street, Downsview, Ontario, Canada, M3H 5T6

INTERFEROMETRIC TECHNIQUES AND DATA EVALUATION METHODS
FOR THE UTIAS 10 cm x 18 cm HYPERVELOCITY SHOCK TUBE

Ben-Dor, G., Whitten, B. T. Approx. 60 pages 14 figures 3 tables

1. Interferometry 2. Shock tubes 3. Measurement error analysis

I. Ben-Dor, G., Whitten, B. T. II. UTIAS Technical Note No. 208

The UTIAS 10 cm x 18 cm Hypervelocity Shock-Tube has been used in recent years to study ionizing shock structures, flat-plate and sidewall boundary layers and nonstationary oblique shock-wave diffractions over compression corners. These phenomena were recorded using a 23-cm dia. field of view Mach-Zehnder interferometer equipped with a giant pulse dual-frequency ruby laser.

In order to extract the maximum amount of data in these complex flows a digital evaluation method was employed. For this technique a new approach to the theory of interference was developed. In this approach the spatial coordinates (x,y) of the various lines of interference (fringes) on the interferograms are put into digital form, thereby making a computer analysis possible.

The experimental technique and instrumentation associated with the various measurements involved in research using the UTIAS 10 cm x 18 cm Hypervelocity Shock-Tube are described. Finally, the maximum possible absolute and relative errors associated with these measurements are calculated for four different gases (argon, krypton, oxygen and nitrogen) which are usually used as test gases.

Available copies of this report are limited. Return this card to UTIAS, if you require a copy.



UTIAS Technical Note No. 208

Institute for Aerospace Studies, University of Toronto (UTIAS)
4925 Dufferin Street, Downsview, Ontario, Canada, M3H 5T6

INTERFEROMETRIC TECHNIQUES AND DATA EVALUATION METHODS
FOR THE UTIAS 10 cm x 18 cm HYPERVELOCITY SHOCK TUBE

Ben-Dor, G., Whitten, B. T. Approx. 60 pages 14 figures 3 tables

1. Interferometry 2. Shock tubes 3. Measurement error analysis

I. Ben-Dor, G., Whitten, B. T. II. UTIAS Technical Note No. 208

The UTIAS 10 cm x 18 cm Hypervelocity Shock-Tube has been used in recent years to study ionizing shock structures, flat-plate and sidewall boundary layers and nonstationary oblique shock-wave diffractions over compression corners. These phenomena were recorded using a 23-cm dia. field of view Mach-Zehnder interferometer equipped with a giant pulse dual-frequency ruby laser.

In order to extract the maximum amount of data in these complex flows a digital evaluation method was employed. For this technique a new approach to the theory of interference was developed. In this approach the spatial coordinates (x,y) of the various lines of interference (fringes) on the interferograms are put into digital form, thereby making a computer analysis possible.

The experimental technique and instrumentation associated with the various measurements involved in research using the UTIAS 10 cm x 18 cm Hypervelocity Shock-Tube are described. Finally, the maximum possible absolute and relative errors associated with these measurements are calculated for four different gases (argon, krypton, oxygen and nitrogen) which are usually used as test gases.

Available copies of this report are limited. Return this card to UTIAS, if you require a copy.



UTIAS Technical Note No. 208

Institute for Aerospace Studies, University of Toronto (UTIAS)
4925 Dufferin Street, Downsview, Ontario, Canada, M3H 5T6

INTERFEROMETRIC TECHNIQUES AND DATA EVALUATION METHODS
FOR THE UTIAS 10 cm x 18 cm HYPERVELOCITY SHOCK TUBE

Ben-Dor, G., Whitten, B. T. Approx. 60 pages 14 figures 3 tables

1. Interferometry 2. Shock tubes 3. Measurement error analysis

I. Ben-Dor, G., Whitten, B. T. II. UTIAS Technical Note No. 208

The UTIAS 10 cm x 18 cm Hypervelocity Shock-Tube has been used in recent years to study ionizing shock structures, flat-plate and sidewall boundary layers and nonstationary oblique shock-wave diffractions over compression corners. These phenomena were recorded using a 23-cm dia field of view Mach-Zehnder interferometer equipped with a giant pulse dual-frequency ruby laser.

In order to extract the maximum amount of data in these complex flows a digital evaluation method was employed. For this technique a new approach to the theory of interference was developed. In this approach the spatial coordinates (x,y) of the various lines of interference (fringes) on the interferograms are put into digital form, thereby making a computer analysis possible.

The experimental technique and instrumentation associated with the various measurements involved in research using the UTIAS 10 cm x 18 cm Hypervelocity Shock-Tube are described. Finally, the maximum possible absolute and relative errors associated with these measurements are calculated for four different gases (argon, krypton, oxygen and nitrogen) which are usually used as test gases.

Available copies of this report are limited. Return this card to UTIAS, if you require a copy.



UTIAS Technical Note No. 208

Institute for Aerospace Studies, University of Toronto (UTIAS)
4925 Dufferin Street, Downsview, Ontario, Canada, M3H 5T6

INTERFEROMETRIC TECHNIQUES AND DATA EVALUATION METHODS
FOR THE UTIAS 10 cm x 18 cm HYPERVELOCITY SHOCK TUBE

Ben-Dor, G., Whitten, B. T. Approx. 60 pages 14 figures 3 tables

1. Interferometry 2. Shock tubes 3. Measurement error analysis

I. Ben-Dor, G., Whitten, B. T. II. UTIAS Technical Note No. 208

The UTIAS 10 cm x 18 cm Hypervelocity Shock-Tube has been used in recent years to study ionizing shock structures, flat-plate and sidewall boundary layers and nonstationary oblique shock-wave diffractions over compression corners. These phenomena were recorded using a 23-cm dia field of view Mach-Zehnder interferometer equipped with a giant pulse dual-frequency ruby laser.

In order to extract the maximum amount of data in these complex flows a digital evaluation method was employed. For this technique a new approach to the theory of interference was developed. In this approach the spatial coordinates (x,y) of the various lines of interference (fringes) on the interferograms are put into digital form, thereby making a computer analysis possible.

The experimental technique and instrumentation associated with the various measurements involved in research using the UTIAS 10 cm x 18 cm Hypervelocity Shock-Tube are described. Finally, the maximum possible absolute and relative errors associated with these measurements are calculated for four different gases (argon, krypton, oxygen and nitrogen) which are usually used as test gases.

Available copies of this report are limited. Return this card to UTIAS, if you require a copy.

UTIAS Technical Note No. 208

Institute for Aerospace Studies, University of Toronto (UTIAS)
4925 Dufferin Street, Downsview, Ontario, Canada, M3H 5T6

INTERFEROMETRIC TECHNIQUES AND DATA EVALUATION METHODS
FOR THE UTIAS 10 cm x 18 cm HYPERVELOCITY SHOCK TUBE

Ben-Dor, G., Whitten, B. T. Approx. 60 pages 14 figures 3 tables

1. Interferometry 2. Shock tubes 3. Measurement error analysis

I. Ben-Dor, G., Whitten, B. T. II. UTIAS Technical Note No. 208

The UTIAS 10 cm x 18 cm Hypervelocity Shock-Tube has been used in recent years to study ionizing shock structures, flat-plate and sidewall boundary layers and nonstationary oblique shock-wave diffractions over compression corners. These phenomena were recorded using a 23-cm dia field of view Mach-Zehnder interferometer equipped with a giant pulse dual-frequency ruby laser.

In order to extract the maximum amount of data in these complex flows a digital evaluation method was employed. For this technique a new approach to the theory of interference was developed. In this approach the spatial coordinates (x,y) of the various lines of interference (fringes) on the interferograms are put into digital form, thereby making a computer analysis possible.

The experimental technique and instrumentation associated with the various measurements involved in research using the UTIAS 10 cm x 18 cm Hypervelocity Shock-Tube are described. Finally, the maximum possible absolute and relative errors associated with these measurements are calculated for four different gases (argon, krypton, oxygen and nitrogen) which are usually used as test gases.

Available copies of this report are limited. Return this card to UTIAS, if you require a copy.



UTIAS Technical Note No. 208

Institute for Aerospace Studies, University of Toronto (UTIAS)
4925 Dufferin Street, Downsview, Ontario, Canada, M3H 5T6

INTERFEROMETRIC TECHNIQUES AND DATA EVALUATION METHODS
FOR THE UTIAS 10 cm x 18 cm HYPERVELOCITY SHOCK TUBE

Ben-Dor, G., Whitten, B. T. Approx. 60 pages 14 figures 3 tables

1. Interferometry 2. Shock tubes 3. Measurement error analysis

I. Ben-Dor, G., Whitten, B. T. II. UTIAS Technical Note No. 208

The UTIAS 10 cm x 18 cm Hypervelocity Shock-Tube has been used in recent years to study ionizing shock structures, flat-plate and sidewall boundary layers and nonstationary oblique shock-wave diffractions over compression corners. These phenomena were recorded using a 23-cm dia field of view Mach-Zehnder interferometer equipped with a giant pulse dual-frequency ruby laser.

In order to extract the maximum amount of data in these complex flows a digital evaluation method was employed. For this technique a new approach to the theory of interference was developed. In this approach the spatial coordinates (x,y) of the various lines of interference (fringes) on the interferograms are put into digital form, thereby making a computer analysis possible.

The experimental technique and instrumentation associated with the various measurements involved in research using the UTIAS 10 cm x 18 cm Hypervelocity Shock-Tube are described. Finally, the maximum possible absolute and relative errors associated with these measurements are calculated for four different gases (argon, krypton, oxygen and nitrogen) which are usually used as test gases.

Available copies of this report are limited. Return this card to UTIAS, if you require a copy.

UNCLASSIFIED
SECURITY CLASSIFICATION OF THIS PAGE (When Data Entered)

REPORT DOCUMENTATION PAGE		READ INSTRUCTIONS BEFORE COMPLETING FORM
1. AFOSR TR-79-0514		2. GOVT ACCESSION NO.
3. TITLE (And Subtitle)		4. TYPE OF REPORT & PERIOD COVERED
6 INTERFEROMETRIC TECHNIQUES AND DATA EVALUATION METHODS FOR THE UTIAS 10 cm x 18 cm HYPERVELOCITY SHOCK TUBE		9 INTERIM / Rept.
5. AUTHOR		6. PERFORMING ORG. REPORT NUMBER
10 G. BEN-DOR B. T. WHITTEN		
7. PERFORMING ORGANIZATION NAME AND ADDRESS		8. CONTRACT OR GRANT NUMBER(s)
UNIVERSITY OF TORONTO INSTITUTE OF AEROSPACE STUDIES, 4925 DUFFERIN ST DOWNSVIEW, ONTARIO, CANADA, M3H 5T6		15 AFOSR-77-3303
9. CONTROLLING OFFICE NAME AND ADDRESS		10. PROGRAM ELEMENT, PROJECT, TASK AREA & WORK UNIT NUMBERS
AIR FORCE OFFICE OF SCIENTIFIC RESEARCH/NA BLDG 410 BOLLING AIR FORCE BASE, D C 20332		10 2307ms 17 A3 61102F
14. MONITORING AGENCY NAME & ADDRESS (if different from Controlling Office)		12. REPORT DATE
14 PUTIAS-TN-2081		11 Mar 1979
		13. NUMBER OF PAGES
		60
15. SECURITY CLASS. (of this report)		
		UNCLASSIFIED
16. DISTRIBUTION STATEMENT (of this Report)		15a. DECLASSIFICATION/DOWNGRADING SCHEDULE
12 62p. Approved for public release; distribution unlimited.		
17. DISTRIBUTION STATEMENT (of the abstract entered in Block 20, if different from Report)		
18. SUPPLEMENTARY NOTES		
19. KEY WORDS (Continue on reverse side if necessary and identify by block number)		
INTERFEROMETRY SHOCK TUBES MEASUREMENT ERROR ANALYSIS		
20. ABSTRACT (Continue on reverse side if necessary and identify by block number)		
The UTIAS 10 cm x 18 cm Hypervelocity Shock Tube has been used in recent years to study ionizing shock structures, flat-plate and side-wall boundary layers and nonstationary oblique shock-wave diffractions over compression corners. These phenomena were recorded using a 23-cm dia field of view Mach-Zehnder interferometer equipped with a giant-pulse dual-frequency ruby laser. In order to extract the maximum amount of data in these complex flows a digital evaluation method was employed. For this technique a new approach to the theory of interference was developed. In this approach the spatial coordinates (x,y) of the various		

lines of interference (fringes) on the interferograms are put into digital form, thereby making a computer analysis possible. The experimental technique, and instrumentation associated with the various measurements involved in research using the UTIAS 10 cm x 18 cm Hypervelocity Shock Tube are described. Finally the maximum possible absolute and relative errors associated with these measurements are calculated for four different gases (argon, krypton, oxygen and nitrogen) which are usually used as test gases. ↙